

# Rotations, Negative Eigenvalues, and Newton Method in Tensor Network Renormalization Group

---

Nikolay Ebel,<sup>a</sup> Tom Kennedy<sup>b</sup> and Slava Rychkov<sup>a</sup>

<sup>a</sup>*Institut des Hautes Études Scientifiques, 91440 Bures-sur-Yvette, France*

<sup>b</sup>*Department of Mathematics, University of Arizona, Tucson, AZ 85721, USA*

*E-mail:* [ebelnikola@gmail.com](mailto:ebelnikola@gmail.com), [slava@ihes.fr](mailto:slava@ihes.fr), [tgk@math.arizona.edu](mailto:tgk@math.arizona.edu)

ABSTRACT: In the tensor network approach to statistical physics, properties of the critical point of a 2D lattice model are encoded by a four-legged tensor which is a fixed point of an RG map. The traditional way to find the fixed point tensor consists in iterating the RG map after having tuned the temperature to criticality. Here we develop a different and more direct technique, which solves the fixed point equation via the Newton method. This is challenging due to the existence of marginal deformations—linear transformations of the coordinate frame, which parametrize a two-dimensional family of fixed points. We address this challenge by including a 90 degree rotation into the RG map. This flips the sign of the problematic marginal eigenvalues, rendering the fixed point isolated and accessible via the Newton method. We demonstrate the power of this technique via explicit computations for the 2D Ising model. Using the Gilt-TNR algorithm at bond dimension  $\chi = 30$ , we find the fixed point tensor with  $10^{-9}$  accuracy, much higher than what was previously achieved.

---

## Contents

<b>1</b>	<b>Introduction</b>	<b>1</b>
<b>2</b>	<b>Intuition for RG eigenvalues</b>	<b>2</b>
2.1	Tensor RG for the 2D Ising	3
2.2	CFT expectations for RG eigenvalues	5
2.3	Symmetry preserved by the RG map	6
2.4	Rotation symmetry breaking and eigenvalues 1	7
2.5	Adding a rotation to the tensor RG map	9
2.6	Newton method	10
<b>3</b>	<b>Results for the non-rotating Gilt-TNR</b>	<b>11</b>
3.1	Review of the non-rotating Gilt-TNR algorithm	12
3.2	Isotropic fixed point by the “shooting” method	13
3.3	Jacobian eigenvalues	18
3.4	Comparison to prior work	20
3.4.1	Locating the fixed point	20
3.4.2	Jacobian eigenvalues	21
3.5	Anisotropy: manifold of fixed points	22
<b>4</b>	<b>Results for the rotating Gilt-TNR</b>	<b>24</b>
4.1	Isotropic fixed point by the Newton method	24
4.2	Anisotropy: period-2 oscillations	30
<b>5</b>	<b>Summary and open problems</b>	<b>30</b>
<b>A</b>	<b>Tensor conventions</b>	<b>33</b>
A.1	Tensor RG	33
A.2	Tensor network symmetries	33
<b>B</b>	<b>Initial tensors for tensor RG evolution</b>	<b>34</b>
<b>C</b>	<b>More details about Gilt-TNR</b>	<b>35</b>
C.1	Dynamic $Q$ -choice	37
C.2	Static $Q$ -choice	38
C.3	Parameter choices and scaling	38
C.4	Gilt-HOTRG [19]	40
<b>D</b>	<b>Gauge fixing</b>	<b>41</b>
D.1	Comment about gauge fixing for $\mathbb{Z}_2$ -odd perturbations	43
D.2	Relation with the approach of Ref. [19]	44
D.3	Why is orthogonal gauge fixing enough?	45

D.3.1	With reflection symmetry	46
D.3.2	Without reflection symmetry	47
<b>E</b>	<b>Gilt-TNR differentiability</b>	<b>48</b>

---

## 1 Introduction

In the last 15 years, the use of tensor networks [1] revolutionized renormalization group (RG) studies of two-dimensional statistical lattice models. Tensor RG<sup>1</sup> maps a tensor network representation of the partition function to an equivalent representation involving a smaller number of tensors. By now there exist many tensor RG algorithms [1–10]. They show excellent numerical performance when benchmarked on exactly solvable two-dimensional models such as Ising or 3-state Potts, truncating to tensors of finite size. In three dimensions, there is currently no fully successful numerical algorithm [5, 10–12]. The analytic theory of tensor RG for infinite-size tensors was initiated in [13, 14] in two dimensions and in [15] in three dimensions.

Here we will be dealing with tensor RG for two-dimensional models. Our main goal will be to introduce a modification of the existing algorithms which allows to recover the critical fixed point tensor. Traditionally, one obtains approximate fixed point tensors by starting from the lattice model at or nearby the exactly known critical temperature and performing a series of 10-20 RG steps, referred below as the “shooting” method. The resulting tensor is close to the fixed point but it is not quite the fixed point, because the irrelevant perturbations have not fully decayed to zero. In this work, we will be able to obtain the fixed point via a Newton method. The Newton method converges provided that the Jacobian has no eigenvalues 1. Naively, there are always perturbations with eigenvalues 1 in our problem. They are associated with aspect-ratio deformations, which break the rotation invariance of the model while keeping criticality. Our main idea will be to change the tensor RG map by including in it a  $\pi/2$  rotation of the lattice. This changes the problematic eigenvalues 1 to  $-1$ , and saves the day for the Newton method.

We will also use the fixed point tensor to extract scaling dimensions of the operators of conformal field theory (CFT) describing the phase transition, and compare with the exact solution. Most tensor RG studies extract the scaling dimensions from the transfer matrix [3] or from the lattice dilatation operator<sup>2</sup> [16]. Here, we will focus on an alternative technique—using the eigenvalues of the tensor RG map linearized around the fixed point (the Jacobian). This is a standard and general RG technique [17, 18], but in the context of tensor RG it has been previously used only a handful of times [19, 20]. (The transfer matrix and the lattice dilatation operator will be studied in the companion paper [21].)

We will encounter two subtle effects when using the Jacobian method:

---

<sup>1</sup>We use this term inclusively, not limited to the first TRG algorithm proposed in [1], but to all RG maps manipulating tensor networks, whether or not they involve disentangling steps or only coarse-graining.

<sup>2</sup>This is the term we propose hoping that it will stick, as there is no generally accepted term.

- The standard relation  $\lambda = b^{d-\Delta}$  between the Jacobian eigenvalues and the scaling dimensions, where  $b > 1$  is the lattice rescaling factor, will be modified by a phase, depending on the spin of the CFT operator under spatial rotations. This extra phase arises due to the  $\pi/2$  rotation present in our map. Thus, some eigenvalues will change sign and some even become complex.
- We will see that the Jacobian eigenvalues of total derivative operators are not universal and not given by the above formula. This is expected from the CFT point of view, but it may be the first time that this is seen in a numerical study. We will provide a reason why Refs. [19, 20] did not observe this effect.

The paper is organized as follows. We start in Section 2 by describing in general terms our problem, possible stumbling blocks, and how we plan to resolve them. In Section 3 we illustrate the intuition developed in Section 2 via concrete calculations using a specific tensor RG map: Gilt-TNR [10]. This map does not include a rotation, thus the Jacobian has eigenvalues 1 at the fixed point, and the Newton method is not applicable. We locate the approximate fixed point using the traditional “shooting” method. We extract scaling dimensions of leading CFT quasiprimaries from the Jacobian eigenvalues at the approximate fixed point. We check that the non-quasiprimary Jacobian eigenvalues are non-universal, i.e. depend on the RG map. Finally, we present evidence for the existence of a manifold of anisotropic fixed points. We then proceed to describe our main new result in Section 4, where we add rotation to the Gilt-TNR map, which turns eigenvalues 1 to  $-1$ . We set up the Newton method and show that it converges. We thus recover the critical isotropic tensor RG fixed point with accuracy  $\sim 10^{-9}$  in the Hilbert-Schmidt distance, much higher than it has ever been achieved and limited only by roundoff and truncation errors. For anisotropic tensors, we exhibit period-2 oscillations of the RG iterates. In Section 5 we conclude and suggest future research directions.

Our paper contains numerous detailed appendices which should be useful to anyone wishing to reproduce or improve our results. In Appendix A we set up the basic conventions concerning tensor RG and symmetries of tensor networks. In Appendix B we discuss how we initialize our tensor RG flow starting from the nearest-neighbor 2D Ising model, including the anisotropic case. Appendix C provides a detailed description of the Gilt-TNR algorithm [10] used here, and of the Gilt-HOTRG algorithm used in [19, 20]. Appendix D describes our continuous and discrete gauge fixing procedures. In Appendix E we provide evidence that the Gilt-TNR map is differentiable near the fixed point, and optimize the step size used to extract the Jacobian via a finite difference approximation.

Much of our work here will be numerical and at an intuitive level of rigor, but we hope that our ideas will also prove useful in the eventual fully rigorous computer-assisted construction of exact tensor network RG fixed points—the program started in [13].

## 2 Intuition for RG eigenvalues

We start with general remarks about tensor RG as applied to the 2D Ising model. We then explain how conformal field theory (CFT) helps classify RG eigenvalues. Finally, we

discuss when the Newton method can and cannot be used to search for the critical RG fixed point. We will see that the Newton method is problematic for non-rotating RG maps which do not preserve rotation symmetry, and we will explain how this problem is solved by adding rotation to the RG map.

## 2.1 Tensor RG for the 2D Ising

We assume that the reader is familiar with the main ideas and terminology of tensor RG, reviewed e.g. in [22]. See also Appendix A.1.

We would like to use tensor RG to study phase transitions and critical points of 2D lattice models. For concreteness we consider the isotropic 2D Ising model with nearest-neighbor ferromagnetic interactions, on the square lattice. The model has a phase transition at  $T = T_c$  separating the ordered and disordered phases. We translate the partition function of the model to a tensor network made of a four-legged tensor  $A^{(0)}$  of bond dimension 2. (See Appendix B for how this is done.) We then pick a tensor RG map  $R$ , and start acting on  $A^{(0)}$  by it repeatedly:

$$A^{(n+1)} = R(A^{(n)}), \quad n = 0, 1, 2, \dots, \quad (2.1)$$

in a way that the partition function is preserved.<sup>3</sup> To preserve the partition function exactly, the bond dimension must be allowed to grow. Tensor RG algorithms truncate the tensor  $A^{(n+1)}$  in such a way that the bond dimension never exceeds a finite number  $\chi$ , a parameter of the algorithm. We would like to take  $\chi$  as large as possible, but this is limited by computational resources; here we will use  $\chi = 30$ .

We assume that all tensors  $A^{(n)}$  are normalized by imposing the unit Hilbert-Schmidt norm:<sup>4</sup>

$$\|A^{(n)}\| = 1. \quad (2.2)$$

We also assume here that the map  $R$  is non-rotating, i.e. it preserves the orientation of the lattice (this will change in Section 2.5). For example, if we apply the map to the tensor network of size  $N \times M$ , then after the RG step the lattice has size  $N/b \times M/b$  where  $b$  is the lattice rescaling factor.

We expect that after many steps this RG evolution will converge to a fixed point, which is a tensor  $A_{\text{fp}}$  satisfying  $R(A_{\text{fp}}) = A_{\text{fp}}$ . In fact we expect 3 fixed point tensors: high-temperature  $A_H$ , low-temperature  $A_L$ , and critical  $A_*$ . The RG evolution starting from  $A^{(0)} = A^{(0)}(T)$  should converge to  $A_H$  for  $T > T_c$ , to  $A_L$  for  $T < T_c$ , and to  $A_*$  for  $T = T_c$  (see Fig. 1).

It is by now known that this expectation can be realized, at least numerically, provided that one uses a tensor RG map with disentangling, so that the CDL problem [23] is solved. There are several algorithms which achieve this [6–10]. The general discussion in this section will apply to any such algorithm. In practical calculations in Section 3 and 4, we will rely on Gilt-TNR [10].

---

<sup>3</sup>More precisely, the partition function is preserved up to a constant related to rescaling the tensor to impose the normalization condition (2.2), see Appendix A.1.

<sup>4</sup>The Hilbert-Schmidt norm of a tensor  $A$  is defined as  $(\sum |A_{ijkl}|^2)^{1/2}$ .

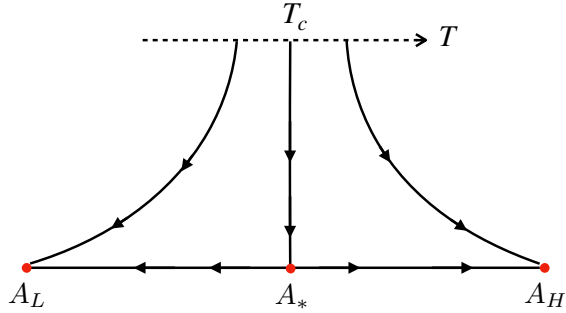


**Figure 1:** Expected pattern of tensor RG evolution for the 2D Ising model. The dashed line is the curve of initial tensors corresponding to varying  $T$  in  $A^{(0)}(T)$ .

As is well-known, tensors  $A_H$  and  $A_L$  in Fig. 1 are simple explicitly known tensors of bond dimension 1 and 2, respectively. Namely,  $A_H$  has a single nonzero tensor element

$$(A_H)_{0000} = 1, \quad (2.3)$$

and tensor  $A_L$  is a direct sum of two copies of  $A_H$ . See [13, 14] for a rigorous theory of tensor RG in the neighborhood of these two fixed points. In this paper, our focus is on the much more interesting and complicated critical fixed point tensor  $A_*$ , which is expected to have infinite bond dimension. To give meaning to infinite sums in the tensor network built out of  $A_*$ , it is natural to require that it be Hilbert-Schmidt, i.e. have a finite Hilbert-Schmidt norm.<sup>5</sup>  $A_*$  is expected to depend on the RG map, although the critical exponents extracted from  $A_*$  should be universal. We would find it surprising if an RG map existed for which  $A_*$  had an explicit expression.<sup>6</sup> In our work we will not aim to find an explicit expression for  $A_*$  but we will compute finite dimensional approximations to  $A_*$  numerically, working at finite  $\chi$ .

According to Fig. 1, to get  $A_*$  approximately one can take the initial tensor  $A^{(0)}$  corresponding to  $T = T_c$  and do several RG iterations.<sup>7</sup> That’s the method used in the prior literature [6–10, 19], which we refer to as “shooting.” (Often the fixed point tensor itself is not exhibited and evidence for reaching the fixed point is presented in the form of gauge-invariant observables reaching limits.) The “shooting” method is limited due to the fact that the RG map is not a contraction in the neighborhood of  $A_*$ . Indeed, the

<sup>5</sup>This is because Hilbert-Schmidt tensors can be contracted along one bond: the result is finite and Hilbert-Schmidt. This implies that the partition function of an  $N \times M$  tensor network built of Hilbert-Schmidt tensors is finite [14], while this property is not guaranteed for tensors which are not Hilbert-Schmidt.

<sup>6</sup>Recently, there were claims of exact tensor network RG fixed points constructed in [24–26]. We find some aspects of those works questionable. In particular it has not been verified that the proposed exact fixed point tensors remain Hilbert-Schmidt when the cutoff is removed. See [27], where we also provide an argument that tensor RG without disentangling cannot have an exact RG fixed point which is Hilbert-Schmidt and corresponds to a nontrivial CFT.

<sup>7</sup>The critical temperature  $T_c$  may be exactly known if the lattice model is exactly solvable, like the nearest-neighbor 2D Ising. In practical calculations at finite  $\chi$ , the critical temperature shifts a bit from the exact one. To find the shifted critical temperature, one may use the bisection method, see footnote 19.

temperature perturbation<sup>8</sup> is relevant, with eigenvalue  $\lambda_t = b^{y_t} > 1$ , where as is well known  $y_t = 1$  (below we recall how this follows from CFT). The number of iterations one can perform is limited by numerical instabilities, and by the residual dependence of  $T_c$  on  $\chi$ . These limitations motivate the goal of our work—to propose an alternative way to get  $A_*$ , via the Newton method.

## 2.2 CFT expectations for RG eigenvalues

The Newton method will involve the Jacobian  $\nabla R$  of the RG map. To set things up, we need to have an idea about the eigenvalues and eigenvectors of  $\nabla R$ . This may be understood with the help of the 2D minimal model CFT  $\mathcal{M}_{3,4}$  which as is well known describes the critical 2D Ising model. Since both the RG fixed point and the CFT describe the same critical state, we expect a broad correspondence between these two descriptions. In particular, perturbations of the RG fixed point  $A_*$  should be in one-to-one correspondence with the local translationally invariant perturbations of the CFT, given by integrals of nontrivial (i.e. excluding the unit operator)<sup>9</sup> CFT local operators:

$$\kappa \int d^2x \mathcal{O}(x). \quad (2.4)$$

On the CFT side, the RG transformation corresponds to rescaling distances  $x \rightarrow bx$ . When we do this, the coupling  $\kappa$  rescales as  $\kappa \rightarrow \lambda\kappa$ , where

$$\lambda = b^{2-\Delta_{\mathcal{O}}}, \quad (2.5)$$

and  $\Delta_{\mathcal{O}}$  is the scaling dimension of  $\mathcal{O}$ . Note that this equation is only significant for operators which are not total derivatives. For  $\mathcal{O}$  a total derivative, perturbation Eq. (2.4) vanishes. Hence, the normalization of  $\kappa$  is ambiguous and  $\lambda$  can be anything.<sup>10</sup>

In summary, CFT predicts that the RG Jacobian  $\nabla R$  at the fixed point  $A_*$  should have a series of eigenvectors in one-to-one correspondence with nontrivial local CFT operators  $\mathcal{O}$ . Eigenvalues of perturbations associated with  $\mathcal{O}$  which are not total derivatives (in CFT parlance such  $\mathcal{O}$  are referred to as quasiprimaries) will be given by Eq. (2.5). Eigenvalues of total derivative perturbations cannot be predicted by general principles; in particular they will depend on the choice of the RG map.

Quasiprimaries of the critical 2D Ising CFT  $\mathcal{M}_{3,4}$  arise as descendants of the three Virasoro primaries  $\mathbb{1}$ ,  $\epsilon$ ,  $\sigma$ . In Table 1 we give the full list of nontrivial quasiprimaries of scaling dimension  $\Delta = h + \bar{h} \leq 5$ , along with their  $\mathbb{Z}_2$ , and spin  $\ell = h - \bar{h}$  quantum numbers.<sup>11</sup> Perturbations corresponding to all these operators should appear among eigenvectors of  $\nabla R$ , with universal eigenvalues. E.g. the eigenvector corresponding to  $\epsilon$  is the temperature perturbation mentioned above:  $\lambda_t = b^{2-\Delta_{\epsilon}} = b$ .

<sup>8</sup>This standard terminology may be a bit confusing, since temperature is a microscopic variable and cannot be varied directly around  $A_*$ . What is meant is that the eigenvector arises from the temperature perturbation of the microscopic tensor  $A^{(0)}(T_c)$  after many RG steps.

<sup>9</sup>Perturbing by the unit operator  $\mathcal{O} = \mathbb{1}$  simply rescales the partition function. In tensor RG, this would translate to rescaling  $A$ . Since we fixed the normalization of  $A$ , Eq. (2.2), such a perturbation will not be present among the  $\nabla R$  eigenvectors.

<sup>10</sup>In the standard RG parlance, perturbation by a total derivative is classified as “redundant” [18].

<sup>11</sup>Many candidate quasiprimaries are null (e.g.  $L_{-2}\epsilon + \dots$ ) and hence do not appear in the table.

	$\mathbb{Z}_2$	$\Delta$	$\ell$
$T, \bar{T}$	+	2	$\pm 2$
$T\bar{T}$	+	4	0
$TT, \bar{T}\bar{T}$	+	4	$\pm 4$
$\epsilon$	+	1	0
$L_{-4}\epsilon + \dots$	+	5	4
$\sigma$	-	0.125	0
$L_{-3}\sigma + \dots$	-	3.125	3

**Table 1:** Critical 2D Ising CFT  $\mathcal{M}_{3,4}$  nontrivial quasiprimary operators of scaling dimension  $\Delta \leq 5$ , with their quantum numbers (see e.g. [28, Table 8.1]).

A second relevant eigenvector corresponds to  $\sigma$ . This eigenvector is however  $\mathbb{Z}_2$ -odd, and thus its existence does not require extra tuning to reach the fixed point. Put another way, in Fig. 1 we were implicitly assuming that the RG map preserves the  $\mathbb{Z}_2$  symmetry of the 2D Ising model. Thus the whole RG evolution happens within the space of  $\mathbb{Z}_2$ -even tensors, with all  $\mathbb{Z}_2$ -odd perturbations set to zero.

Let’s discuss the interplay of tensor RG and symmetry in more detail.

### 2.3 Symmetry preserved by the RG map

The 2D Ising model has a global on-site  $\mathbb{Z}_2$  (spin flip) symmetry. It is also invariant under spatial symmetry transformations, which in the isotropic case form the group  $D_4$  generated by the axis reflections and  $\pi/2$  rotations.<sup>12</sup> Translating the model to a tensor network, one naturally obtains a tensor  $A^{(0)}$  which is invariant under all these symmetries. See Appendix A.2 for a recap of symmetries of tensor networks.

Suppose we have a tensor RG map  $R$  which preserves symmetry  $G$ , which means that the subspace  $\mathcal{T}^G$  of  $G$ -invariant tensors is invariant under  $R$ . Then, if the initial tensor  $A^{(0)}$  is  $G$ -invariant, the whole RG evolution (2.1) happens within the  $G$ -invariant subspace  $\mathcal{T}^G$ . We can also look for a fixed point  $A_*$  within  $\mathcal{T}^G$ . This is convenient for several reasons. First, because it implies a reduction in the number of variables to consider. Second, because we do not have to worry about relevant or marginal directions orthogonal to  $\mathcal{T}^G$ .

Preserving on-site symmetries such as the Ising spin-flip is easy—all tensor RG maps naturally achieve this. This is reflected in Fig. 1, as mentioned at the end of Section 2.2.

On the other hand, it turns out to be hard to implement disentangling while preserving rotations. Available tensor RG maps with disentangling preserve reflections along one axis

<sup>12</sup>By spatial symmetry we mean point group symmetry. Lattice translational symmetry is always present and is left implicit. For unequal horizontal and vertical nearest-neighbor couplings  $J_x \neq J_y$ , spatial symmetry gets reduced to a smaller group. The final spatial symmetry depends on whether the reduction of the spin model to a tensor network is performed rotating by  $\pi/4$  not. In this paper we will study the case  $J_x \neq J_y$  with  $\pi/4$  rotation, see Appendix B.



[6], along both axes [9, 29, 30], or no spatial symmetry at all [7, 8, 10].<sup>13</sup> Gilt-TNR [10], which we will use in practical calculations, belongs to the last group of algorithms.

For such RG maps, even though the initial tensor respects a spatial symmetry, we cannot impose it on subsequent tensors along the RG evolution. Also the critical fixed point tensor cannot be expected to have a spatial symmetry, and indeed our numerical calculations will show that it does not. This may seem puzzling because of course the critical point should enjoy the same spatial symmetry as the original tensor, and indeed a larger one because it should be fully  $O(2)$  rotationally symmetric. But there is no contradiction: this simply means that the spatial symmetry of the critical point is not manifest.

One may consider this an inconvenience but not necessarily a problem from the practical point of view. And indeed this did not impede the prior tensor RG work, which found the approximate critical fixed point tensor via shooting from  $A^{(0)}(T_c)$ . However for our goal of using the Newton method this turns out to be a problem, as we will now explain.

## 2.4 Rotation symmetry breaking and eigenvalues 1

According to Table 1, the Jacobian  $\nabla R$  at the fixed point will have two eigenvectors which are marginal, i.e. have eigenvalues 1. These eigenvectors are associated with the CFT stress tensor holomorphic and antiholomorphic components  $T, \bar{T}$ . In the real stress tensor component basis, we can associate these eigenvectors with the linear combinations

$$T_{11} - T_{22} \quad \text{and} \quad T_{12}, \quad (2.6)$$

conveniently aligned with the coordinate axes  $x_1, x_2$  which we identify with the two axes of the tensor network. (Recall that the stress tensor trace  $T_{11} + T_{22}$  vanishes in a CFT.)

Consider deforming the CFT by the stress tensor perturbation  $\int d^2x h_{\mu\nu} T^{\mu\nu}$  with an  $x$ -independent  $h_{\mu\nu}$ . This deforms the 2D metric:  $\delta_{\mu\nu} \rightarrow g_{\mu\nu} = \delta_{\mu\nu} + h_{\mu\nu}$ . Physically, this deforms the rotational symmetry of the critical point, turning circles  $|x| = 1$  into ellipses  $|x|_g = 1$  where  $|x|_g$  is the distance computed with respect to the  $g_{\mu\nu}$  metric. For example the two-point correlation functions in the deformed theory will scale as powers of  $|x|_g$ . The first perturbation in (2.6) gives an ellipse whose axes are aligned with the coordinate axes, which breaks  $\pi/2$  rotations but preserves axis reflections. The second perturbation gives a tilted ellipse and breaks both rotations and reflections. These deformations make sense for infinitesimal and for finite  $h_{\mu\nu}$ . We will call the ellipse  $|x|_g = 1$  the anisotropy ellipse. Because of scale invariance, the overall scale of the anisotropy ellipse does not play a role, so it is characterized by two parameters, e.g. the main axes ratio and the tilt angle.

Even though the above perturbations break rotations, they preserve criticality, since the correlation length remains infinite. We expect a two-dimensional manifold  $\mathcal{M}_2$  of corresponding RG fixed points, in one-to-one correspondence with possible anisotropy ellipses. The critical fixed point  $A_*$  in Fig. 1 is but one point of  $\mathcal{M}_2$ . The complete picture looks like in Fig. 3. The discussed perturbations with eigenvalues 1 span the tangent space of  $\mathcal{M}_2$ .

---

<sup>13</sup>The isotropic TNR scheme from [22, App. C] would preserve rotation symmetry. This complicated map acts on networks built of three different tensors. To our knowledge it has not been implemented in practice.

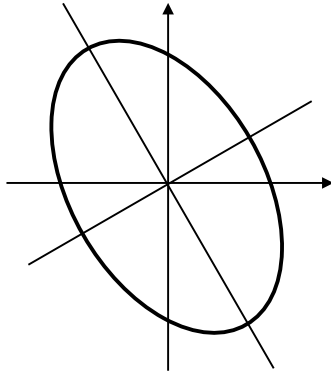


**Figure 2:** Anisotropy ellipse parametrizing translationally invariant stress-tensor perturbations of the CFT.

Note that the anisotropy ellipse is a physical quantity which can be associated with any critical tensor, whether it is a fixed point or not. We should just compute two-point correlation functions at large distances and see for which metric  $g$  they scale as powers of  $|x|_g$ . Defined this way, the anisotropy ellipse is an RG invariant on the critical manifold for the kind of RG maps we are considering (non-rotating RG maps changing both lattice dimensions by the same factor  $b$ ), and all points on the RG trajectory will have the same anisotropy ellipse as the initial critical tensor. In the case at hand the initial tensor represents the nearest-neighbor isotropic Ising model on the square lattice, for which the anisotropy ellipse is of course the circle. So, the same will be true for the fixed point  $A_*$  which we will therefore call “isotropic fixed point”. The previous observation explains why RG iterations get attracted to a single fixed point rather than start wandering around the fixed point manifold  $\mathcal{M}_2$ .

Now that we know that the fixed point  $A_*$  is isotropic, does this help us to find it? The answer would be yes if we had a tensor RG algorithm preserving lattice rotation symmetry. In that case we could be sure that  $A_*$  belongs to a subspace of rotation-symmetric tensors. We could restrict RG evolution to this subspace, within which  $\nabla R$  would be free of eigenvalues 1. It would have been trivial then to set up the Newton method. But in the absence of manifest rotation symmetry, the situation is not so rosy. Even though  $A_*$  is isotropic, there is nothing manifestly special about  $A_*$  as a tensor which could help us to limit the search. We are forced to work in a larger space of all tensors, which contains the above perturbations, and hence  $\nabla R$  will have eigenvalues 1.<sup>14</sup>

Now, it is well known that eigenvalues 1 present a problem for solving a fixed point equation via the Newton method. At an intuitive level, the problem can be explained as follows. If the Newton method does work, we can rewrite the fixed point equation in an equivalent form so that the map becomes a contraction in a neighborhood of the solution. A contraction has a unique fixed point. Thus, we conclude that the solution must be isolated. However we have seen that the solution is not isolated—there is a manifold of

<sup>14</sup>If we used a tensor RG algorithm preserving one or both axis reflections, such as [6, 9, 29, 30], we could project out the second perturbation in (2.6), but the first one would still be present.

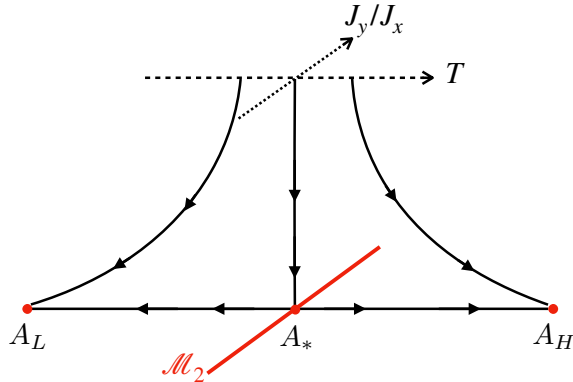


**Figure 3:** This figure corrects Fig. 1 to show that we expect a two-dimensional manifold  $\mathcal{M}_2$  of fixed point tensors. (Since two of the three dimensions in the figure represent directions orthogonal to the fixed point manifold, we had to represent  $\mathcal{M}_2$  by a one-dimensional thick red line.) Microscopically, we may consider the anisotropic 2D Ising model with varying  $J_y/J_x$ . Tensor RG flows starting from the critical point of this model (dotted line) will be attracted to a one-dimensional submanifold of  $\mathcal{M}_2$ . Adding the next to nearest neighbor interaction we may cover the whole  $\mathcal{M}_2$ .

fixed points. This contradiction shows that there must be an obstruction to setting up the Newton method. In Section 2.6 we will see the problem more clearly from a formal point of view. But first let us discuss how we will solve the problem and get rid of eigenvalues 1.

## 2.5 Adding a rotation to the tensor RG map

In the discussion so far, we assumed (Section 2.1) that the tensor RG map  $R$  is non-rotating, i.e. it preserves the orientation of the underlying lattice. This was needed e.g. when applying the prediction (2.5) for RG eigenvalues to perturbations associated with CFT operators with spin, like the stress tensor. We saw that such maps have features (eigenvalues 1 and a manifold of fixed points) which are problematic for our goal of using the Newton method. To solve this problem, we propose to consider rotating RG maps, which change the orientation. Concretely, we will consider a tensor RG map  $R^\circ$  which is a composition of a non-rotating map  $R$ , followed by  $\Gamma_{\pi/2}$ , rotation of the tensor by  $\pi/2$ :

$$R^\circ = \Gamma_{\pi/2} R, \quad (2.7)$$

or graphically:

$$\text{Diagram of } R^\circ(A) = \text{Diagram of } R(A) \quad (2.8)$$

So, the rotating map  $R^\circ$  maps a tensor network of size  $N \times M$  to one which has size  $M/b \times N/b$ , see Eq. (A.3):

$$\begin{array}{ccc}
 N & \xrightarrow{R^\circ} & M/b \\
 \color{blue}{\square} & & \color{blue}{\square} \\
 M & & N/b
 \end{array} . \tag{2.9}$$

Adding a rotation to the RG map may appear strange, and indeed recognizing that this is useful is the main idea of our paper.<sup>15</sup>

Starting from the isotropic 2D Ising tensor  $A^{(0)}(T)$ , the RG evolution of  $R^\circ$  is expected to show the same pattern of fixed points as that of  $R$  in Fig. 1. In particular, the flow from  $A^{(0)}(T_c)$  will lead to a critical isotropic fixed point tensor, which we denote  $A_*^\circ$ . (Note that  $A_*^\circ \neq A_*$ , the fixed point tensor of  $R$ , because  $R$  does not preserve rotations.) Jacobian eigenvalues around the fixed point  $A_*^\circ$  can be computed using the CFT data, up to a change having to do with the rotation. On the CFT side, a spin  $\ell$  operator  $\mathcal{O}$  transforms under rotation by angle  $\theta$  as

$$\mathcal{O} \mapsto e^{i\theta\ell} \mathcal{O}. \tag{2.10}$$

In our case  $\theta = \pi/2$ . This implies that Eq. (2.5) for the Jacobian eigenvalues needs to be modified in case of  $R^\circ$  as follows:

$$\lambda = (i)^{\ell\circ} b^{2-\Delta\circ}. \tag{2.11}$$

Applying this to the CFT stress tensor which has spin  $\pm 2$ , we conclude that the eigenvectors of  $\nabla R^\circ$  corresponding to the stress tensor components  $T, \bar{T}$  will have eigenvalues  $-1$ , and not 1 as for  $\nabla R$ . Relatedly, when extended to anisotropic and not-rotationally invariant tensors, the map  $R^\circ$  will not have a two-dimensional manifold of fixed points as  $R$  did, Fig. 3. Instead, the isotropic fixed point  $A_*^\circ$  will be isolated, and its neighborhood will contain a two-parameter manifold of period-2 orbits of  $R^\circ$ .

Eigenvalues  $-1$  pose no problem for the Newton method, and we expect to use the Newton method to find the fixed point  $A_*^\circ$  of  $R^\circ$ . We stress that the fixed point  $A_*^\circ$  of  $R^\circ$  is as good as  $A_*$  of  $R$  for describing the critical point physics. It is only that  $A_*^\circ$  can be found using the Newton method, while  $A_*$  cannot.

## 2.6 Newton method

Let us finally set up the Newton method. As mentioned, we will be solving the fixed point equation  $R^\circ(A) = A$ , which has an isolated solution at  $A_*^\circ$ . We rewrite the equation as

$$f(A) = 0, \quad \text{where } f(A) = A - R^\circ(A). \tag{2.12}$$

<sup>15</sup>The earliest tensor RG map [1] did change the orientation, however the point we will make—that this eliminates eigenvalues 1—did not play a role in that pioneering paper which was focused on other issues.

The Newton method solves the latter equation via iterations<sup>16</sup>

$$A_{(m+1)} = g(A_{(m)}), \quad \text{where } g(A) = A - [J(A)]^{-1}f(A), \quad (2.13)$$

and  $J(A) = I - \nabla R^\circ(A)$  is the Jacobian of the map  $f$ .

As discussed,  $\nabla R^\circ(A_*^\circ)$  does not have eigenvalues 1. This implies that  $J(A_*^\circ)$  is invertible and  $g(A)$  is well defined in a neighborhood of  $A_*^\circ$ .<sup>17</sup> Furthermore, if we compute  $\nabla g$  and evaluate it at  $A_*^\circ$  using  $f(A_*^\circ) = 0$ , we find

$$\nabla g(A_*^\circ) = 0. \quad (2.14)$$

This implies in particular that  $g(A)$  is a contraction near  $A_*^\circ$ . Therefore, Newton iterations (2.13) will converge for a sufficiently good initial approximation.

The Jacobian  $J(A)$  entering the definition of  $g(A)$  is rather expensive to evaluate and invert, so we will replace it by a constant matrix  $J_\approx$  which approximates  $J(A_*^\circ)$ . In other words we will use the approximate Newton map

$$g_\approx(A) = A - [J_\approx]^{-1}f(A), \quad (2.15)$$

For any invertible  $J_\approx$  the solutions of  $f(A) = 0$  and  $g_\approx(A) = A$  coincide. We will be solving the latter equation by iterations. We just need to choose  $J_\approx$  so that  $g_\approx$  is a contraction near  $A_*^\circ$ . The following approximation works well in practice. Let  $A_{(0)}$  be a tensor sufficiently close to  $A_*^\circ$ . Diagonalize  $\nabla R^\circ(A_{(0)})$ , arrange eigenvalues in the order of decreasing absolute value, and let  $P_s$  be the orthogonal projector on the subspace spanned by the first  $s$  eigenvectors. We will use

$$J_\approx = I - P_s \nabla R^\circ(A_{(0)}) P_s. \quad (2.16)$$

We must have  $s \geq 3$ , so that the relevant eigenvalue corresponding to the  $\epsilon$  and the two  $-1$  eigenvalues corresponding to  $T, \bar{T}$  are subtracted. We will see below that taking  $s > 3$  speeds up convergence.

*Remark 2.1.* In this section by the Jacobian we meant the Jacobian restricted to the subspace of  $\mathbb{Z}_2$ -even tensors. Thus, only  $\mathbb{Z}_2$ -even Jacobian eigenvalues play a role in the considerations concerning the Newton method. Below, when extracting the CFT spectrum from the linearized RG map, we will also consider the Jacobian in the  $\mathbb{Z}_2$ -odd subspace.

### 3 Results for the non-rotating Gilt-TNR

We now proceed to concrete tensor RG computations, based on the Gilt-TNR algorithm. We will start in this section with several in-depth studies using the original Gilt-TNR algorithm, which is non-rotating. We will thus be able to compare with the prior work

<sup>16</sup>To distinguish them better, we use superscripts to number RG iterates (2.1) and subscripts for Newton iterates.

<sup>17</sup>On the contrary, if we try to apply this to  $R$  instead of  $R^\circ$ ,  $\nabla R$  has eigenvalues 1,  $J$  is not invertible, and the Newton method fails.

from Refs. [10, 19, 20], and to test various intuitions about tensor RG from Section 2, such as the existence of marginal eigenvalues corresponding to the stress-tensor deformations, and of a manifold of fixed points corresponding to different anisotropy parameters. We will also test the Jacobian method for extracting CFT scaling dimensions. After this thorough warm-up, in the next section we will switch to the rotating Gilt-TNR algorithm, and present our main numerical result: find the fixed point via the Newton method.

*Remark 3.1.* Before we start, the following comment is in order. In the previous section, when we discussed the conceptual picture, the fixed points  $A_*$  or  $A_*^\circ$  denoted exact fixed points of the exact non-rotating or rotating RG map. From now on we will be discussing numerical RG maps operating at a finite bond dimension  $\chi$ . The logic of the previous section should still apply to some approximation, but of course the fixed points will have finite bond dimension and will be different from  $A_*$  and  $A_*^\circ$ . To stress this we will denote the fixed points as  $A_*^{[\chi]}$  and  $A_*^{\circ[\chi]}$ . Our goal here will be to extract these fixed points as precisely as possible, for a finite  $\chi$ . What happens with  $A_*^{[\chi]}$  and  $A_*^{\circ[\chi]}$  as  $\chi \rightarrow \infty$ , whether they converge to  $A_*$  or  $A_*^\circ$ , is a separate and very interesting question which is beyond the scope of this work.

### 3.1 Review of the non-rotating Gilt-TNR algorithm

The original, non-rotating, Gilt-TNR RG map [10] is defined as follows. Take a group of four contracted  $A$  tensors inside the tensor network (a plaquette). One starts by inserting on the contracted bonds matrices  $Q_1, \dots, Q_4$  chosen so that the insertion 1) leaves the contraction intact (approximately); 2) eliminates short-range CDL-like correlations around the plaquette. How to choose the  $Q_i$ 's is the trademark of the algorithm, see [10] and Appendix C. Performing a singular value decomposition (SVD) of each  $Q_i$  matrix, we get the following result:

$$A \approx Q_4 Q_1 Q_2 Q_3 \stackrel{\text{svd}}{=} \text{SVD decomposition}, \quad (3.1)$$

where the light-brown shading represents CDL-like correlations.

We now perform the above replacement, with the same  $Q_1, \dots, Q_4$ , to every second plaquette of the tensor network, in a checkerboard pattern. We then contract the half-tensors with the  $A$ 's, defining two tensors  $B_1$  and  $B_2$  as:

$$B_1 = \text{tensor with green and pink}, \quad B_2 = \text{tensor with yellow and cyan}. \quad (3.2)$$

The original tensor network made of  $A$  is thus mapped to a tensor network made of  $B_1$

and  $B_2$ , which has CDL-like correlations eliminated on every other plaquette:

(3.3)

This finishes the disentangling stage of Gilt-TNR.

The second stage of Gilt-TNR is coarse-graining. The default coarse-graining strategy of our code [31] is via two consecutive TRG [1] iterations:

$$\text{TRG}_1 : B_1, B_2 \mapsto C, \quad \text{TRG}_2 : C \mapsto \tilde{A}, \quad (3.4)$$

Namely,  $\text{TRG}_1$  performs SVD-decompositions of  $B_1$  and  $B_2$  diagonally, and then recombines the SVD pieces into a tensor  $C$ , so that CDL-like correlations remaining in (3.3) are contracted away:

(3.5)

Analogously,  $\text{TRG}_2$  performs an SVD-decomposition of  $C$  diagonally in two different ways and defines a tensor  $\tilde{A}$  by recombining the pieces. The point is that after  $\text{TRG}_1$  there are no CDL-like correlations in the networks, and so it makes sense to follow up with  $\text{TRG}_2$  right away before any further disentangling.<sup>18</sup> A moment’s thought shows that after the two TRG iterations the lattice ends up rotated by  $\pi/2$ . Since the original Gilt-TNR code [32] aims to be non-rotating, the third and final stage of Gilt-TNR is to define the RG-transformed tensor  $A'$  by rotating  $\tilde{A}$  back to recover the original orientation.

The map  $\mathcal{R} : A \mapsto A'$  is the non-normalized Gilt-TNR map. The corresponding normalized RG map  $R(A)$  is defined by  $R(A) = A'/\|A'\|$ . The lattice rescaling factor is  $b = 2$ .

### 3.2 Isotropic fixed point by the “shooting” method

Most of our work in this section will be for the 2D Ising model which is isotropic, i.e. has equal nearest-neighbor couplings  $J_x = J_y$  (only in Section 3.5 we will consider the anisotropic case). We transform the partition function of the isotropic model to a tensor network. There are many ways to do this; we use the way detailed in Appendix B. The resulting tensor  $A_{\text{NN}}(t)$  has bond dimension 2. We parametrize it by the reduced temperature  $t = T/T_c$  where  $T_c$  is the critical temperature.

We thus have the tensor  $A^{(0)} = A_{\text{NN}}(t)$  to which we start applying the non-rotating Gilt-TNR algorithm, obtaining a sequence of tensors  $A^{(n)}$ ,  $n = 1, 2, \dots$ , see Eq. (2.1). Our

<sup>18</sup>We thank Clément Delcamp for explaining this point and for passing to us a minimal working version of the original Gilt-TNR code [32] where the described strategy is realized.

first goal is to verify the picture from Fig. 1. To see that a tensor  $A^{(n)}$  converges to a fixed point we need to apply gauge-fixing after each RG step, as explained below. But as a proxy, to detect fixed point behavior, it is standard to use gauge-invariant observables. One such set of observables are the singular values of  $A^{(n)}$  decomposed along a diagonal:

$$\text{---} \overset{A}{\bullet} \text{---} \stackrel{\text{svd}}{=} \overset{U}{\text{---}} \overset{\Lambda}{\text{---}} \overset{V}{\text{---}}. \quad (3.6)$$

Here  $U, V$  are unitaries and  $\Lambda$  is a diagonal matrix of singular values. In Fig. 4 we plot the singular values, normalized by the largest singular value, as a function of the RG step. The RG evolution was started at  $t = 1.0000110043$ , the value found by bisecting<sup>19</sup> up to  $\Delta t = 10^{-10}$ , to maximize the length of the plateaux visible in Fig. 4, whose presence signals that the RG evolution nears the fixed point, before visibly deviating from it for  $n \gtrsim 30$ . In the plotted case,  $t$  happens to be slightly below the true  $t_c$  for the chosen Gilt-TNR parameters, and one can see that the deviation happens in the direction of the low-temperature phase where the fixed point tensor  $A_{*L}$  has two identical singular values, all other ones being equal to zero. For  $t$  slightly above  $t_c$  one observes similar plateaux with eventual deviation towards the high-temperature phase where the fixed point tensor  $A_{*H}$  has a single nonzero singular value. Our Fig. 4 compares well e.g. with the results reported in:

- [10, Fig. 6] using the non-rotating Gilt-TNR;
- [19, Fig. 9] for another closely related non-rotating algorithm Gilt-HOTRG;
- [33, Fig. 6, two upper panels] for Loop-TNR [7] and NNR-TNR.

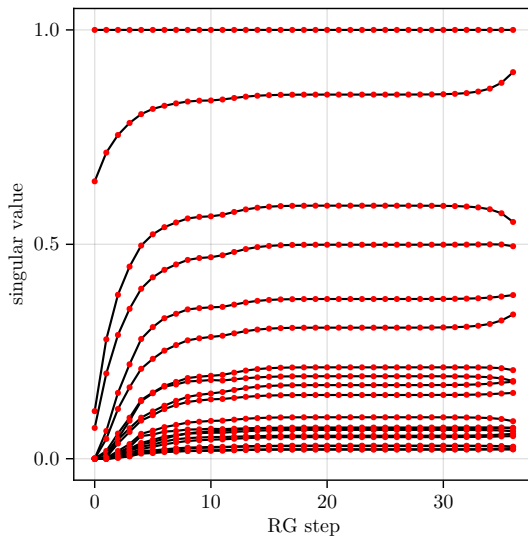
The plateau in Fig. 4 is a strong indication that the family of tensors  $A^{(n)}$  approaches a common gauge equivalence class, so that the gauge invariant observables do converge. Next, we would like to see this explicitly, by choosing a gauge for each tensor  $A^{(n)}$  so that gauge-fixed tensors tend to a limit, in the Hilbert-Schmidt norm. This limit is then a fixed-point tensor. Our gauge-fixing procedure is described in Appendix D. It involves two steps: continuous gauge fixing followed by discrete gauge fixing. Continuous gauge fixing matrices are obtained from diagonalizing appropriate environments constructed out of  $A^{(n)}$ . Discrete gauge fixing consists in multiplying by diagonal matrices with  $\pm 1$  on the diagonal.

Fig. 5 demonstrates the stated convergence of the gauge-fixed RG flow to the fixed point. In this figure, we plot the Hilbert-Schmidt distance between gauge-fixed tensors  $A^{(n)}$

---

<sup>19</sup>As mentioned in footnote 7, the critical temperature will shift from the exact  $t_c = 1$  when working at finite bond dimension. To locate the finite- $\chi$  critical temperature, one uses the bisection algorithm: 1) Start from a ‘bracketing interval’  $I = [t_l, t_h]$  such that  $t_l$  is in the low-temperature phase and  $t_h$  is in the high-temperature phase; 2) Test the midpoint of the interval  $I$  - which phase is it in? This is done by running tensor RG for several steps until the tensor starts approaching the high-temperature or lower-temperature fixed points, which can be noticed by monitoring the singular values computed as in (3.6); 3) Bisection: depending on the outcome of 2), replace the interval  $I$  by its lower or upper half  $I'$  whose endpoints are in different phases; 4) Repeat the above 3 steps until the bracketing interval has length smaller than the required accuracy  $\Delta t$ .





**Figure 4:** The RG flow of tensors starting from  $A^{(0)}$  corresponding to the Ising model at the reduced temperature  $t = 1.0000110043$  and with anisotropy  $J_x/J_y = 1$  (i.e. the isotropic tensor), in terms of the 20 largest singular values along the diagonal, Eq. (3.6), normalized by the first one. Gilt-TNR parameters (see Table 4):  $\chi = 30$ ,  $\epsilon_{\text{gilt}} = 6 \times 10^{-6}$ .

and  $A^{(n+1)} = R(A^{(n)})$  as a function of the RG step.<sup>20</sup> We see that the distance decreases until  $n \sim 23$  and then starts increasing. The decrease and increase of the distance are rather smooth,<sup>21</sup> showing that our gauge-fixing procedure works well. The increase of the distance for  $n \gtrsim 23$  is roughly consistent with the leading RG eigenvalue being  $\lambda = b^{2-\Delta_\epsilon} = 2$ . This eigenvalue corresponds to the CFT quasiprimary  $\epsilon$ .

On the other hand the convergence rate for  $n \lesssim 23$  roughly agrees with the largest irrelevant RG eigenvalue in the  $\mathbb{Z}_2$ -even sector being  $\lambda_{\text{irr}} \approx 0.63$  as we will see below when studying the Jacobian eigenvalues (Table 3, column “ $\lambda$  of  $\nabla R$ ”). This eigenvalue does not correspond to a quasiprimary, the leading irrelevant quasiprimary being  $T\bar{T}$  of dimension 4 and eigenvalue 0.25. Although this eigenvalue corresponds to a total derivative operator, it does control the rate of approach to the fixed point.

The following general analysis is instructive. Given the critical temperature to  $\Delta t$  accuracy, and the leading irrelevant  $\mathbb{Z}_2$ -even eigenvalue  $\lambda_{\text{irr}}$ , which is the optimal number of steps  $n_*$  for the shooting method, and which accuracy  $\delta_*$  of approximating the fixed point tensor we may expect? Basic RG intuition says that after  $n$  steps, the fixed point tensor is approximated by

$$\delta_n \sim \max((\lambda_{\text{irr}})^n, (\Delta t)2^n), \quad (3.7)$$

where we use that the relevant  $\mathbb{Z}_2$ -even eigenvalue is  $\approx 2$ . Minimizing this expression over

<sup>20</sup>To compute the distance between tensors  $A^{(n)}$  with  $n \leq 10$  we applied additional relative discrete gauge fixing (akin to that used in [19]), as using  $I_+$  evaluated at the tensor approximating the critical one was not enough to bring tensors close to each other (see Appendix D).

<sup>21</sup>Except for a blip around step 11 where a small irregularity is also seen in the singular values, Fig. 4.

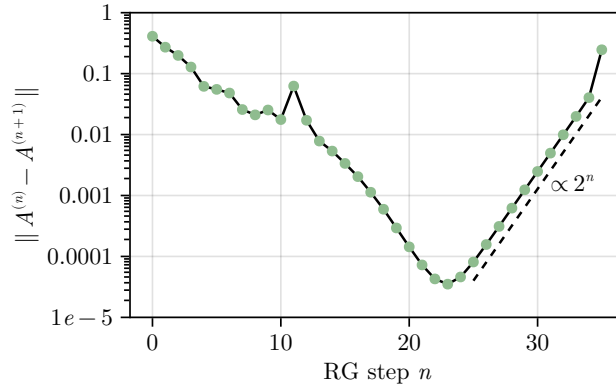


**Figure 5:** The Hilbert-Schmidt distance between two subsequent gauge-fixed tensors as a function of the RG step. Gilt-TNR parameters are the same as in Fig. 4.

$n$  we get

$$n_* \sim -\frac{\log_2 \Delta t}{1 - \log_2 \lambda_{\text{irr}}}, \quad \delta_* \sim \Delta t^{\frac{1}{1 - \log_2 \lambda_{\text{irr}}}}. \quad (3.8)$$

For  $\lambda_{\text{irr}} = 0.63$ ,  $\Delta t = 10^{-10}$ , we get  $n_* \sim 20$ ,  $\delta_* \sim 10^{-4}$ , in reasonable agreement with Fig. 5.

In Section 3.4, we will compare our Fig. 5 to the results of [19, 20], who also considered the norm difference of two consecutive tensors.

Let us discuss next the tensor elements of the approximate fixed point tensor, defined as the tensor  $A^{(n)}$  with  $n = n_*$  corresponding to the minimum in the curve in Fig. 5. From the above discussion we expect that  $A^{(n_*)}$  approximates the fixed point  $A_*^{[30]}$  of the  $\chi = 30$  Gilt-TNR map<sup>22</sup> with accuracy

$$\|A^{(n_*)} - A_*^{[30]}\| \sim 5 \times 10^{-5}. \quad (3.9)$$

It is also interesting to record the distance from the critical nearest-neighbor Ising tensor from which we started the RG evolution:

$$\|A^{(n_*)} - A_{\text{NN}}(1)\| \approx 0.90. \quad (3.10)$$

The first few largest tensor elements of  $A^{(n_*)}$  are reported in Table 2, Column 2. (Column 3 of the same table gives the approximate fixed point tensor of the RG map with rotation, to be discussed in Section 4. Please ignore them for now.)

We divided the tensor elements of  $A^{(n_*)}$  in Table 2 into several groups. If the fixed point tensor preserved reflection and/or rotation invariance, tensor elements in each group would be equal, perhaps up to a sign. Instead, we see that the tensor elements within groups are close but not exactly equal. How should we interpret this? Recall that we started the RG evolution from the isotropic tensor  $A^{(0)}$  which is reflection and rotation invariant. However,

<sup>22</sup>See Remark 3.1. Apart from  $\chi = 30$ , the fixed point  $A_*^{[30]}$  also depends of course on other parameters of Gilt-TNR such as  $\epsilon_{\text{gilt}}$  but we leave this dependence implicit.

$ijkl$	$(A^{(n_*)})_{ijkl}$	$(A_{(m_*)})_{ijkl}$
1+1+1+1+	0.3411	0.3520
1+1+1-1-	0.2107	0.2119
1-1+1+1-	0.2105	0.2027
1-1-1+1+	0.1969	0.2042
1+1-1-1+	0.1971	0.2135
1-1-1-1-	0.1807	0.1829
1+1-1+1-	0.1481	0.1474
1-1+1-1+	0.1438	0.1503
1+1+2-2-	-0.1067	-0.1056
2-1+1+2-	0.1068	0.1024
1+2-2-1+	0.1015	0.1069
2-2-1+1+	-0.1016	-0.1033
1-1+1-2+	0.1048	0.08593
2+1-1+1-	0.08648	0.08152
1+1-2+1-	0.08705	0.09959
1-2+1-1+	0.07821	0.08898

**Table 2:** The first few largest tensor elements of the (approximate) fixed point tensor. The tensor legs are ordered as left-top-right-bottom. The leg indices are numbered in the notation  $p^\pm$  where  $\pm$  is the  $\mathbb{Z}_2$  quantum number and  $p = 1, 2, 3, \dots$  is the index in the corresponding  $\mathbb{Z}_2$  sector on the corresponding leg. Column 1: tensor element indices. Column 2: the approximate fixed point tensor  $A^{(n_*)}$  of the non-rotating Gilt-TNR. Column 3: the approximate fixed point tensor  $A_{(m_*)}$  of the rotating Gilt-TNR, to be discussed in Section 4.

as we already mentioned, Gilt-TNR does not preserve these symmetries (although it does preserve the spin flip  $\mathbb{Z}_2$ ). That's why the fixed point tensor in Table 2 does not respect these symmetries.<sup>23</sup>

In Fig. 6 we show absolute values of tensor elements of approximate fixed point tensors for  $\chi = 30$  as well as for  $\chi = 10, 20$ , for comparison.<sup>24</sup> Absolute values of tensor elements are sorted in descending order and indexed as  $|A|_I$  where  $I = 1, 2, \dots$  is the position in the sorted list. We then plot  $|A|_I$  as a function of  $I$ . The left figure shows the first 50 tensor elements, while the right figure gives a global of view of all tensor elements, in the

<sup>23</sup>One can also see from Table 2 that the horizontal reflection is broken by a smaller amount than rotations and the vertical reflection. E.g. in column 2 we have  $A_{1+1+1-1-} \approx A_{1-1+1+1-}$ ,  $A_{1-1-1+1+} \approx A_{1+1-1-1+}$  (horizontal reflections) hold to a much better accuracy than say  $A_{1+1+1-1-} \approx A_{1-1-1+1+}$  (vertical reflection). A likely reason for this is given in footnote 36.

<sup>24</sup>For  $\chi = 10, 20$  we follow the same procedure as for  $\chi = 30$ . First, we find approximate  $t_c$  by bisecting to  $10^{-10}$  and looking for the longest plateau in singular values as in Fig. 4. We find  $t_{\chi=10} = 1.0012778632$  ( $\epsilon_{\text{gilt}} = 10^{-4}$ ) and  $t_{\chi=20} = 1.0000618664$  ( $\epsilon_{\text{gilt}} = 2 \times 10^{-5}$ ). Then, we produce a plot of Hilbert-Schmidt distances between subsequent gauge-fixed tensors, as in Fig. 5. The approximate fixed point tensor is defined as  $A^{(n)}$  corresponding to the minimum of this plot.

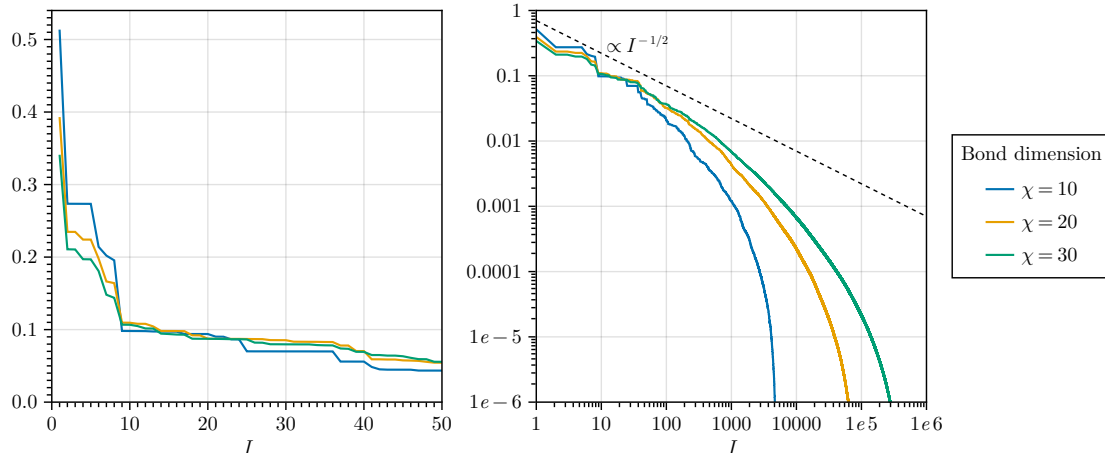


**Figure 6:** Absolute values of tensor elements of approximate fixed point tensors for  $\chi = 10, 20, 30$ , see the text.

log-log scale. The dashed line in this figure corresponds to the slope  $|A|_I \sim I^{-1/2}$ , which marks the boundary for the finiteness of the Hilbert-Schmidt norm for infinite-dimensional tensors. It is reassuring that the fixed point tensors seem to remain below that line as  $\chi$  is increased, although barely so.

### 3.3 Jacobian eigenvalues

Now that we provided evidence for the existence of a fixed point tensor, we would like to explore the RG map Jacobian at the approximate fixed point. First of all we can speak of the Jacobian as our map is differentiable in a neighborhood of the fixed point. Evidence for this is provided in Appendix E. This statement is less trivial than it may seem. To make Gilt-TNR robustly differentiable we had to tweak the algorithm a bit. In the original Gilt-TNR (see Appendix C where this is referred to as “dynamic  $Q$ -choice”), matrices  $Q_1, Q_2, Q_3, Q_4$  are chosen iteratively, and the number of iterations is determined at runtime depending on a certain internal parameter called  $\epsilon_{\text{conv}}$ . For constant  $\epsilon_{\text{conv}}$ , the number of iterations may jump for small variations of tensor  $A$  causing a tiny but noticeable discontinuity (and hence non-differentiability) in  $\mathcal{R}(A)$ . To avoid this problem, we are using a modified algorithm in which the number of iterations is kept fixed, referred to as “static  $Q$ -choice” in Appendix C.<sup>25</sup>

So, let  $R$  be the non-rotating Gilt-TNR RG map with  $\chi = 30$  and other parameters as in Fig. 4. Let  $\nabla R$  be the Jacobian of  $R$  at the tensor  $A^{(n_*)}$  from Table 2. We are interested in the eigenvalues of  $\nabla R$ .

<sup>25</sup>Other tensor RG algorithms involving disentanglers, such as e.g. TNR [6], also involve iterative optimization of disentanglers, to minimize a cost function expressing a truncation error. It would be interesting to see if those algorithms are, or may be made, continuous or differentiable in a small neighborhood of the critical fixed point. To our knowledge this has never been tested carefully.

$\mathbb{Z}_2$	$\mathcal{O}$	$\lambda_{\text{CFT}} = 2^{2-\Delta_{\mathcal{O}}}$	$\lambda$ of $\nabla R$	$\lambda$ of $\nabla R^\circ$
+	$\epsilon$	2	1.9996	1.9996
+	$T$	1	1.0015	-1.0010
+	$\bar{T}$	1	0.9980	-0.9982
+			0.6322	0.7757
+			$0.5941 \pm 0.1195i$	0.6209
			...	...
-	$\sigma$	$2^{15/8} \approx 3.668016$	3.6684	3.668014
-			1.5328	$0.0027 \pm 1.5364i$
-			1.5300	0.8600
-			0.8869	$0.6318 \pm 0.0583i$
			...	...

**Table 3:** Column 1:  $\mathbb{Z}_2$  quantum number. Column 2,3 (colored rows): the first few low-dimension CFT quasiprimaries, and their exact eigenvalues. Columns 4,5: The first few largest, in absolute value, Jacobian eigenvalues at the approximate fixed point for the non-rotating Gilt-TNR ( $\nabla R$ ) and for the rotating Gilt-TNR ( $\nabla R^\circ$ ). Uncolored rows show RG eigenvalues corresponding to derivative interactions, which are not universal.

Note that tensor  $A^{(n_*)}$  preserves  $\mathbb{Z}_2$  flip symmetry, in the sense that each of its vertical and horizontal indices can be assigned a  $\pm 1$  quantum number, such that the tensor remains invariant when acted upon by all these sign flips, i.e., the tensor is  $\mathbb{Z}_2$ -even.<sup>26</sup>

The full tangent space at  $A^{(n_*)}$ , on which  $\nabla R$  acts, splits into a direct sum of subspaces of perturbations which are  $\mathbb{Z}_2$ -even and  $\mathbb{Z}_2$ -odd. Since  $R$  preserves  $\mathbb{Z}_2$ ,  $\nabla R$  maps  $\mathbb{Z}_2$ -even perturbations to  $\mathbb{Z}_2$ -even, and similarly for  $\mathbb{Z}_2$ -odd. Each eigenvector will be either  $\mathbb{Z}_2$ -even or  $\mathbb{Z}_2$ -odd.

The first few largest eigenvalues of  $\nabla R$  at  $A^{(n_*)}$  are reported in Table 3, column “ $\lambda$  of  $\nabla R$ .” Since  $\nabla R$  is a large matrix of size  $\chi^4 \times \chi^4$ , its full diagonalization would be too time consuming. We use Krylov’s method implemented in a Julia [34, 35] package `KrylovKit.jl` [36]. A nice feature of Krylov’s method is that it does not require evaluation and storage of the full matrix  $\nabla R$ . Instead, one provides a function  $v \mapsto \nabla R.v$ , which computes the directional derivative of  $R$  in the direction  $v$ . We evaluate this directional derivative via a symmetric finite difference approximation:

$$D_h = \frac{R(A + hv) - R(A - hv)}{2h}, \quad (3.11)$$

where  $h = 10^{-4}$  is a small parameter, set at this value to balance truncation and roundoff errors; see Appendix E.

Colored rows of Table 3 correspond to CFT quasiprimaries. The corresponding Jacobian eigenvalues can be compared to the CFT predictions in columns 2,3, computed via

<sup>26</sup>A tensor  $A$  is  $\mathbb{Z}_2$ -even or  $\mathbb{Z}_2$ -odd if  $A_{ijkl} s_i s_j s_k s_l = \pm A_{ijkl}$  where  $s_i, s_j, s_k, s_l$  are the quantum numbers of the four legs and the sign  $\pm$  is  $+$  for even,  $-$  for odd.

Eq. (2.5). We observe reasonably good agreement, both in the  $\mathbb{Z}_2$ -even and in the  $\mathbb{Z}_2$ -odd sectors. Note in particular the two eigenvalues close to 1 corresponding to the stress tensor components  $T$  and  $\bar{T}$ .

In the few uncolored rows in Table 3 we report eigenvalues which do not correspond to quasiprimaries on the CFT side. These rows correspond to derivative operators, whose eigenvalues are not universal, as discussed in Section 2.2. For this reason, the CFT entries in these rows are left empty.<sup>27</sup>

To demonstrate the latter point, let us compare the Jacobian eigenvalues between  $R$  and the rotating Gilt-TNR map  $R^\circ$  which will be discussed in Section 4 (Table 3, last column). We see that the quasiprimary eigenvalues change very little, apart from the  $-1$  factor picked up by the  $T$ ,  $\bar{T}$  eigenvalues, as discussed in Section 2.5. On the other hand, several eigenvalues in the uncolored rows show significant changes. For example, the leading irrelevant  $\mathbb{Z}_2$ -even eigenvalue  $\lambda_{\text{irr}}$  changes from  $\approx 0.63$  to  $\approx 0.78$ .

The spectrum of even lower eigenvalues beyond those shown in Table 3 becomes rather messy. Unfortunately we do not have enough precision to compare with the irrelevant quasiprimaries in the  $\mathbb{Z}_2$ -even and  $\mathbb{Z}_2$ -odd sectors. Their eigenvalues are buried among the non-universal eigenvalues corresponding to derivative operators.

### 3.4 Comparison to prior work

Our results in Sections 3.2 and 3.3 can be compared with the results of Ref. [19, 20]. We will divide the comparison into two parts: locating the fixed point via the “shooting” method, and computing the Jacobian eigenvalues.

#### 3.4.1 Locating the fixed point

Ref. [19, 20] are the first works which implemented a gauge fixing procedure and plotted the norm difference of two consecutive tensors as a function of the RG step to produce a plot like our Fig. 5.<sup>28</sup>

Ref. [19] used an algorithm closely related to Gilt-TNR, which we call Gilt-HOTRG, as it uses Gilt for disentangling, and HOTRG for coarse-graining (see Appendix C.4). It is an algorithm closely related to Gilt-TNR. Several parameter choices were identical for us and for them:  $\chi = 30$ ,  $\epsilon_{\text{gilt}} = 6 \times 10^{-6}$ .

Ref. [20] also used essentially Gilt-HOTRG with some minor modifications. They use  $\chi = 24$ ,  $\epsilon_{\text{gilt}} = 2 \times 10^{-7}$ . They also split an RG step in two and only use disentangling on odd steps. This doubling of the number of steps should be kept in mind when comparing with the plots of [20].

Ref. [19] used gauge fixing similar to the one used by us, while Ref. [20] used a more sophisticated two-step gauge fixing. In the first step they gauge fix by general invertible

---

<sup>27</sup>Note that the Jacobian matrix is real but in general not symmetric, and so some eigenvalues come in complex-conjugate pairs.

<sup>28</sup>Previously, some works [6, 8, 16] said they could reach an approximate fixed point tensor by gauge fixing, but without a plot like Fig. 5 the accuracy is hard to know. Ref. [33] quantified the rate of convergence to the fixed point by plotting the norm difference of the vectors of singular values for consecutive tensors as a function of the RG step, but without performing gauge fixing.

matrices to achieve the Minimal Canonical Form (MCF) [37], which minimizes the norm of the gauge-fixed tensor. In the second step they gauge fix by orthogonal matrices, similarly to [19] (with some improvements) and to us.

The norm-difference plot [20, Fig. 3, red curve], is rather similar in shape to our Fig. 5, although their minimal distance  $\delta \sim 3 \times 10^{-4}$  is larger than our  $\delta \sim 5 \times 10^{-5}$ . This may be due to them locating the critical temperature not as precisely as us.

On the other hand the norm difference plot [19, Fig. 9(b)] reaches a much worse minimal distance  $\delta \sim 10^{-2}$  in spite of them locating the critical temperature to the same  $\Delta t = 10^{-10}$  accuracy as us. Ref. [20] investigated this issue. In their Fig. 13 they reproduce the results of [19] and note that the rate of approach to the fixed point tensor is notably slower for the algorithm of [19] than for their algorithm. In the language of Section 3.2, we could say that the algorithm of [20] has  $\lambda_{\text{irr}}$  about the same as our algorithm, while the algorithm of [19] has  $\lambda_{\text{irr}}$  closer to 1. This interpretation is conjectural since [19, 20] don't report their  $\lambda_{\text{irr}}$ .

Therefore, the MCF step in gauge fixing, is the only significant difference between the algorithms of Refs. [19] and [20], is responsible for the improvement of the convergence rate to the fixed point in their case. On the other hand it should be noted that our algorithm is able to reach the same convergence rate without MCF but using Gilt-TNR instead of Gilt-HOTRG. There is a little bit of luck involved here, the leading irrelevant eigenvalue  $\lambda_{\text{irr}}$  being non-universal.

### 3.4.2 Jacobian eigenvalues

In Section 3.3 we studied the Jacobian of Gilt-TNR close to the critical point. In particular, we reported the leading irrelevant eigenvalue  $\lambda_{\text{irr}}$  and observed that the rate of approach to the fixed point is consistent with it. Since Refs. [19, 20] do not report the spectrum of the Jacobian of the map used to produce their norm-difference plots, the  $\lambda_{\text{irr}}$  test is not possible based on their available data. Such a test would be interesting in the future.

Refs. [19, 20] do study the spectrum of a tensor RG map Jacobian (procedure called there “linearized tensor RG”, or “ITRG”), but only for a different RG map, constructed once the (approximate) fixed point is known. This new “frozen” (our term) RG map has the Gilt disentanglers and the HOTRG isometries frozen to their fixed point values.<sup>29</sup>

Ref. [19] uses the spectrum of the frozen RG map Jacobian to extract the scaling dimensions of CFT operators with  $\Delta \leq 2$  [19, Table I], and Ref. [20] extends this analysis to  $\Delta \leq 3$  [20, Table I]. Compared to our  $\nabla R$  spectrum, their accuracy is one order of magnitude worse for  $\sigma$  and  $\epsilon$ , and is about the same for  $T, \bar{T}$ . Our better performance for  $\sigma$  and  $\epsilon$  may be due to our better approximation of the fixed point tensor.

Their results contain one curious feature: in addition to quasiprimaries  $\sigma, \epsilon, T, \bar{T}$ , it contains many derivative operators identified with first and second derivatives of  $\sigma, \epsilon$  and first derivatives of  $T, \bar{T}$ , whose scaling dimensions are correctly reproduced (up to numerical errors) from frozen RG eigenvalues. This is puzzling: we emphasized many

---

<sup>29</sup>The change in the RG map can be inferred from the linearization expression [19, Eq. (40)] and is also stated explicitly in [20] below Eq. (18).

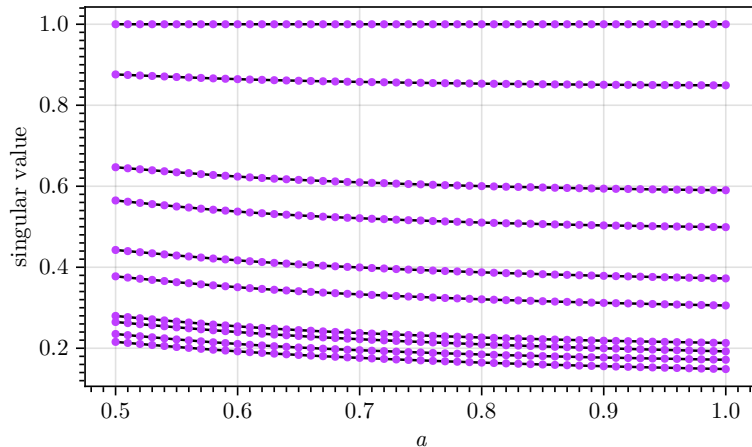


**Figure 7:** Dependence of the first few singular values of  $A^{(20)}(t \approx t_c(a), a)$  on  $a$ . The singular values are obtained via SVD decomposition as in Eq. (3.6). The largest singular value is normalized to 1 as in Fig. 4.

times that eigenvalues of derivative operators are not universal and do not have to agree between RG and CFT, and indeed they do not agree for us. So why do they agree for them? This was not discussed in [19, 20].

The answer to this puzzle is instructive. It turns out that the frozen RG map of [19, 20] is very special: its Jacobian coincides with the lattice dilatation operator. This coincidence, which does not hold for our RG maps  $R$  and  $R^\circ$ , explains the puzzle, because lattice dilatation operator eigenvalues are universal and reproduce all CFT operator eigenvalues, including total derivatives. It would require too much preparatory work to explain this point in detail here; it will be done in [21].

### 3.5 Anisotropy: manifold of fixed points

In the previous sections we studied the RG flow starting from the isotropic 2D Ising model. We would now like to show the new features which appear when introducing anisotropy. Namely, we consider the nearest neighbor Ising model with anisotropy parameter  $a = J_y/J_x \leq 1$ . We transform the partition function of this model to a tensor network as detailed in Appendix B. The resulting tensor has bond dimension 2 and depends on the reduced temperature  $t$  and the anisotropy parameter  $a$ . Starting from this tensor  $A^{(0)} = A_{\text{NN}}(t, a)$  we repeatedly apply the non-rotating Gilt-TNR algorithm to get a sequence  $A^{(n)}(t, a)$ ,  $n = 1, 2, \dots$ , see Eq. (2.1).

We have two goals in this section: 1) We want to verify Fig. 3 showing that  $a$  parametrizes a one-dimensional manifold of fixed points. To our knowledge, this has never been checked using tensor RG. 2) We want to demonstrate that eigenvalues of  $\nabla R$  corresponding to quasiprimaries are universal across this manifold and eigenvalues that do not correspond to quasiprimaries can vary.



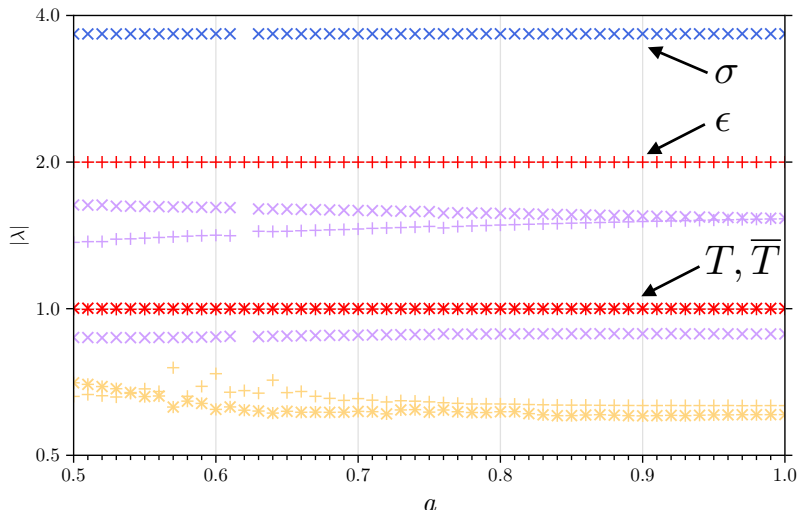


**Figure 8:** The first few largest eigenvalues of  $\nabla R$  computed at  $A^{(20)}(t \approx t_c(a), a)$  as a function of the anisotropy parameter  $a$ . Note the vertical  $\log_2$ -scale. We use the following color scheme: red/blue for  $\mathbb{Z}_2$ -even/odd quasiprimaries, light-orange/light-violet for other  $\mathbb{Z}_2$ -even/odd eigenvalues. For  $a = 1$  the spectrum agrees with the “ $\lambda$  of  $\nabla R$ ” column of Table 3.

Let us start with the first goal. As discussed in Section 2.4 we expect a two-dimensional manifold of RG fixed points for a non-rotating RG map. The critical model corresponds to  $t = 1$  in our notation, for all values of  $a$ . However, as in the isotropic case, for finite bond dimension the value of  $t$  that gives convergence to the approximate fixed point is not exactly 1 and will depend on  $a$ . We denote it by  $t_c(a)$ .<sup>30</sup> If we start with a critical anisotropic nearest neighbor Ising model ( $t = t_c(a)$ ), then iterations of the RG map will converge to a fixed point that depends on the anisotropy parameter  $a$ . To show that different values of  $a$  do indeed produce different fixed points, we consider the singular values of the fixed point decomposed along a diagonal as defined in Eq. (3.6). If we plot these singular values as a function of the RG step, we see curves that are qualitatively similar to Fig. 4. In particular for  $t \approx t_c(a)$  there is a range of RG steps where the singular values are almost constant. However, these constant values depend on  $a$ . We compute these singular values at the 20th RG step for  $a$  ranging from 0.5 to 1.0 and  $t \approx t_c(a)$ , and plot them as a function of  $a$  in Fig. 7. The variation of these values with  $a$  shows that as we vary  $a$ , the RG fixed point is varying along a one-dimensional manifold. We expect that by considering a more general initial Ising model with two parameters we could obtain the full two-dimensional manifold of fixed points.

Let us proceed with the second goal. As discussed in Section 2.2 the eigenvalues of the RG Jacobian  $\nabla R$  should be of two types: those that correspond to quasiprimaries in the CFT and those that correspond to total derivatives. The former are given by Eq. (2.5) and

<sup>30</sup>Approximate values of  $t_c(a)$  were obtained by the bisection method as explained after Eq. (3.6) with  $\Delta t = 10^{-10}$ .

so should not depend on which fixed point in the two-dimensional manifold we consider. The latter cannot be predicted from the CFT and may depend on the fixed point at which we compute the Jacobian. In Fig. 8 we plot the first few eigenvalues of  $\nabla R$  as a function of  $a$ . The eigenvalues corresponding to quasiprimaries are shown in red/blue for the  $\mathbb{Z}_2$ -even/odd sectors. These eigenvalues are essentially independent of  $a$  and fit the CFT predictions of  $2^{15/8}$ , 2 and 1 very well. The eigenvalues corresponding to total derivatives are shown in light-orange/light-violet for the  $\mathbb{Z}_2$ -even/odd sectors. For these eigenvalues one can see significant variation with  $a$ . For  $a = 1$  the spectrum agrees with the “ $\lambda$  of  $\nabla R$ ” column of Table 3.<sup>31</sup>

We thus see broad agreement with the intuition expounded in Section 2.

*Remark 3.2.* In Fig. 8 there are no  $\mathbb{Z}_2$ -odd eigenvalues shown for  $a = 0.62$ . For this value of  $a$  the computation of the  $\mathbb{Z}_2$ -odd eigenvalues produced nonsensical results which we do not show. We believe that this is a result of the issues with discrete gauge fixing in the  $\mathbb{Z}_2$ -odd sector that are discussed in Appendix D.1.

## 4 Results for the rotating Gilt-TNR

Here we will finally present what we consider our most exciting numerical results. We will consider the rotating Gilt-TNR algorithm. We will describe how the critical fixed point is found with the Newton method, in agreement with the general discussion in Section 2. We will study the rate of convergence of the Newton method, and we will use the fixed point to extract CFT quasiprimary dimensions using the Jacobian. All the above will be done in Section 4.1 for the isotropic Ising model case, and the discussion here will parallel Sections 3.2 and 3.3 for the non-rotating algorithm. We will consider the anisotropic case in Section 4.2 where we exhibit period-2 oscillations for the rotating Gilt-TNR algorithm when starting from an anisotropic critical tensor.

### 4.1 Isotropic fixed point by the Newton method

So let  $R^\circ$  be the rotating Gilt-TNR map, constructed by adding a  $\pi/2$  rotation to the non-rotating Gilt-TNR. The numerical results below are obtained using the same Gilt parameters as in Section 3.2:  $\chi = 30$ ,  $\epsilon_{\text{gilt}} = 6 \times 10^{-6}$ .

We would like to solve the fixed point equation for  $R^\circ$  via the Newton method. We set up the Newton method as described in Section 2.6. The key ingredients here are the Jacobian  $\nabla R^\circ$  and its eigendecomposition, which are computed similarly to the non-rotating Gilt-TNR, Section 3.3.

Ideally, we would like the Newton method to converge to the fixed point when starting from a generic point on the critical manifold, e.g. from the bond dimension 2 tensor  $A_{\text{NN}}(t = 1)$  obtained when translating the critical isotropic 2D Ising model to the tensor network form (Appendix B). In practice however our Newton method seems to have a smaller

---

<sup>31</sup>For all values of  $a$  in Fig. 8 there is a pair of complex-conjugate eigenvalues in the lower part of the plot. For most values of  $a$  the pair is the 9th and 10th eigenvalues, but for a few values of  $a$  it is the 8th and 9th. For complex eigenvalues we plot their absolute value. Since the two eigenvalues in this pair have the same absolute value, the result is an “ $\times$ ” and a “ $+$ ” right on top of each other.

neighborhood of convergence. Because of this our search for the fixed point consists of two stages:

1. Find an approximate fixed point tensor  $A^{(n')}$ , obtained by performing  $n' = 23$  RG steps starting from  $A_{\text{NN}}(t)$ , where  $t$  is near the finite- $\chi$  critical temperature  $t_c \approx 1$ , obtained by the bisection method with  $\Delta t = 10^{-10}$ .<sup>32</sup>
2. Start Newton iterations from  $A^{(n')}$ , which are then seen to converge to a fixed point.

Denoting  $A_{(0)} = A^{(n')}$ , the Newton iterations are given by

$$A_{(m+1)} = g_{\approx}(A_{(m)}), \quad n = 0, 1, 2, \dots, \quad (4.1)$$

where  $g_{\approx}$  is the approximate Newton map from Eq. (2.15). The approximate Jacobian  $J_{\approx}$  is evaluated at  $A_{(0)}$ , as in Eq. (2.16), with projector rank  $s \geq 3$  as discussed there. We will see below how various choices of  $s$  influence the performance.

Before starting the Newton iterations, it is instructive to consider  $\nabla R^{\circ}$  eigenvalues at  $A_{(0)}$ . Recall (Table 3, column 3) that  $\nabla R$  had two eigenvalues close to 1 at  $A^{(n_*)}$ : 1.0015 and 0.9980. In Section 2.5 we argued that adding the rotation should flip the sign of the two eigenvalues 1, which are associated with the stress tensor components. Our numerical check fully confirms that intuition: we find that  $\nabla R^{\circ}(A_{(0)})$  has precisely 2 eigenvalues close to  $-1$ :  $-1.0006$  and  $-0.9985$ , and no eigenvalues close to 1.

Given this encouraging news, we expect Newton iterations (4.1) to converge, and this is indeed what we observe numerically. Fig. 9 demonstrates the rate of convergence, for several projector ranks  $s = 3, 9, 26, 54$ . In that plot, we show the Hilbert-Schmidt distance  $\|A_{(m+1)} - A_{(m)}\|$  as a function of the Newton iteration number  $m = 0, 1, 2, \dots$ . We see exponential convergence for all values of  $s$ , improving for larger  $s$ . Recall that the finite-dimensional Newton method is expected to converge super-exponentially fast if at iteration  $m$  we use  $J = I - \nabla R^{\circ}(A_{(m)})$  instead of  $J_{\approx}$  in Eq. (2.15). Using  $J_{\approx}$  reduces the convergence to exponential. As usual, the rate of the exponential convergence can be understood in terms of the largest eigenvalue of the Jacobian of the map  $g_{\approx}(A)$  at the fixed point. Actually, the convergence rate improvement with  $s$  seen in Fig. 9 saturates around the maximal  $s = 54$  used in that figure. At the end of this section we will give a more detailed discussion of the convergence rate, to understand why it first improves with  $s$  and then saturates, and how to improve it further.

Whatever  $s$ , the exponential convergence stops and is replaced by a chaotic behavior when  $\|A_{(m+1)} - A_{(m)}\|$  becomes  $\sim 10^{-9}$  or a bit smaller (for  $s = 3$  this happens outside of the shown range of  $m$ ). We assign this behavior to roundoff errors. In Appendix E, we provide evidence that Gilt-TNR has roundoff order  $\sim 10^{-11}$ . It is not unreasonable that this error is enhanced to  $\sim 10^{-9}$  in the Newton method due to additional involved operations, such as evaluating the Jacobian.

---

<sup>32</sup>Tensor  $A^{(n')}$  in this section should not be confused with tensor  $A^{(n_*)}$  in Section 3.2. They are different tensors because the RG map is different. Also,  $n_* = 23$  in Section 3.2 which was chosen to minimize  $\|R(A^{(n)}) - A^{(n)}\|$ , while here we choose  $n' = 23$  simply as a sufficiently large number.

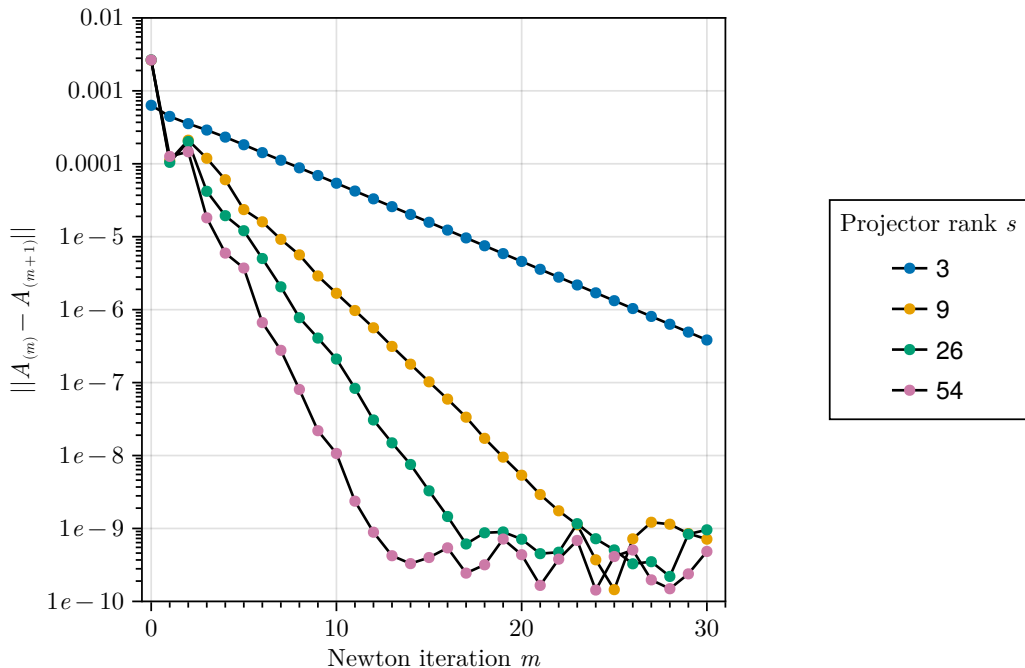


**Figure 9:** Convergence of the Newton method for approximations of Jacobian that use different rank  $s$  of the  $P_s$  projector in Eq. (2.16).

All tensors corresponding to points at the bottom of Fig. 9 should approximate the critical tensor equally well. We have checked their pairwise distances and they are all  $\sim 10^{-9}$ , see Fig. 10.

For further numerical tests we consider the  $s = 54$  Newton iteration sequence and pick from it the tensor  $A_{(m_*)}$  with  $m_* = 14$ , which is the last iteration when  $\|A_{(m+1)} - A_{(m)}\|$  decreases. From the above discussion, we expect that  $A_{(m_*)}$  is an excellent approximation to the (unique) fixed point  $A_*^{\circ[30]}$  of rotating  $\chi = 30$  Gilt-TNR (for the given Gilt parameters), with error

$$\|A_{(m_*)} - A_*^{\circ[30]}\| \sim 10^{-9}. \quad (4.2)$$

Applying the RG map to  $A_{(m_*)}$ , we obtain that this shifts the tensor by

$$\|R^\circ(A_{(m_*)}) - A_{(m_*)}\| \approx 3 \times 10^{-10}, \quad (4.3)$$

providing a further check of (4.2). We also report the distance from the initial tensor for Newton iterations

$$\|A_{(m_*)} - A_{(0)}\| \approx 3 \times 10^{-3}, \quad (4.4)$$

which gives an idea of the size of the convergence domain for our implementation of the Newton method, as well as the distance from the critical nearest-neighbor Ising tensor

$$\|A_{(m_*)} - A_{\text{NN}}(1)\| \approx 0.89. \quad (4.5)$$

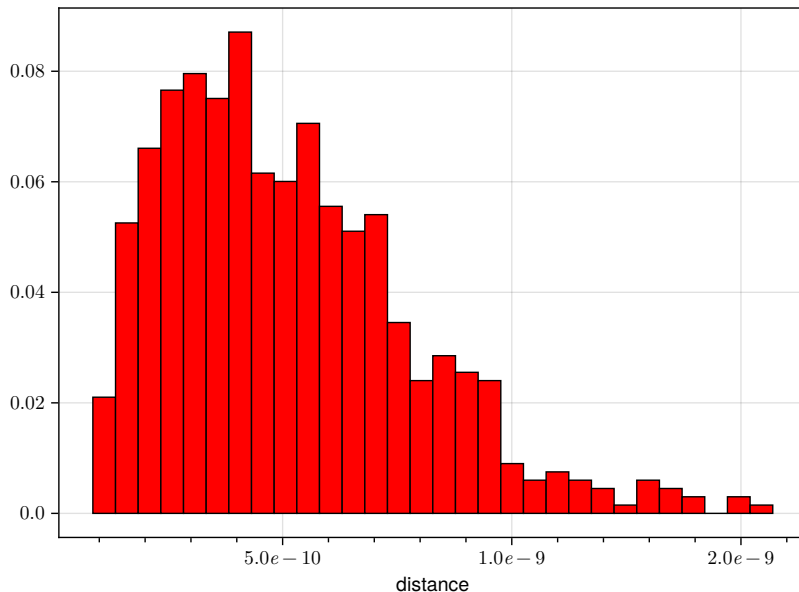


**Figure 10:** The histogram of distances between the 37 tensors in Fig. 9 which fall below the  $10^{-9}$  line.

In Table 2, last column, we show the first few tensor elements of  $A_{(m_*)}$ . We see that they are rather similar, although not identical, to those of  $A^{(n_*)}$ , the approximate fixed point tensor of the non-rotating Gilt-TNR. The distance is, see Fig. 11:

$$\|A_{(m_*)} - A^{(n_*)}\| \approx 0.18. \quad (4.6)$$

This is in agreement with our general intuition that while the critical exponents are universal, RG fixed points are not—different RG maps will in general have different fixed points.

Just like  $A^{(n_*)}$ , tensor  $A_{(m_*)}$  does not respect reflections and rotations. The general comments in this regard made in Section 3.2 still apply. We found that the distribution of tensor elements in their absolute magnitude has the same general shape for  $A_{(m_*)}$  as for  $A^{(n_*)}$ , so we do not repeat Fig. 6.

Let us next discuss the eigenvalues of the Jacobian  $\nabla R^\circ$  at  $A_{(m_*)}$ . The first few largest eigenvalues are reported in Table 3, last column. The main point here is that the quasiprimary eigenvalues are in good agreement with the CFT and with the observation that  $T, \bar{T}$  eigenvalues should flip sign.

Tensor  $A_{(m_*)}$  is a much better approximation for the fixed point of rotating Gilt-TNR than  $A^{(n_*)}$  was for the non-rotating Gilt-TNR ( $10^{-9}$  vs  $5 \times 10^{-5}$ , Eq. (3.9)). Does this lead to a better agreement of quasiprimary eigenvalues with CFT? Comparing the  $\nabla R$  and  $\nabla R^\circ$  columns of Table 3, we see that  $\sigma$  eigenvalue agreement improves by two orders of magnitude, while  $\epsilon, T, \bar{T}$  eigenvalues do not improve. Apparently, the error in these eigenvalues is dominated by the finite- $\chi$  truncation effects, and not by the error in the

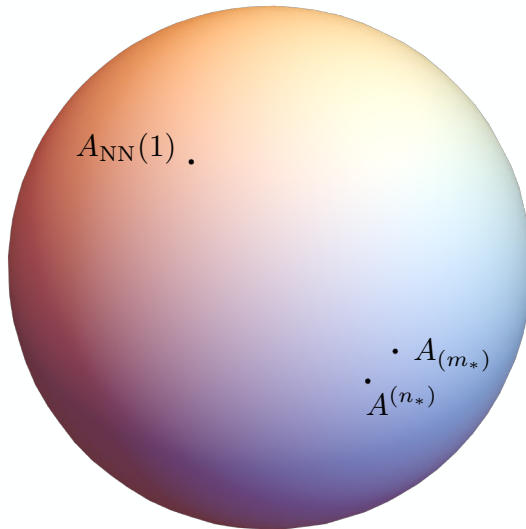


**Figure 11:** The geometry on the unit Hilbert-Schmidt sphere corresponding to the distances (3.10),(4.5),(4.6). The Hilbert-Schmidt sphere has large dimension, but since there are three tensors involved, the geometry can be shown on a two-dimensional unit sphere as in this figure.

determination of the finite- $\chi$  fixed point tensors. It is not clear to us why the  $\sigma$  eigenvalue is special in this regard.

As for the non-rotating case, we also see in Table 3 a bunch of non-universal eigenvalues of  $\nabla R^\circ$ , associated with derivative interactions. Of some interest here is the leading irrelevant  $\mathbb{Z}_2$ -even eigenvalue  $\lambda_{\text{irr}} \approx 0.78$ , as it would control the rate of approach to the fixed point if the traditional “shooting” method were used instead of the Newton method, see Remark 4.1 below.

Another curious observation may be made about the subleading  $\mathbb{Z}_2$ -odd eigenvalues  $0.0027 \pm 1.5364i$ , which are very close in absolute value to the pair of subleading  $\mathbb{Z}_2$ -odd eigenvalues 1.5328 and 1.5300 of  $\nabla R$  reported in the same table, but are almost imaginary rather than real. It is tempting to speculate that these eigenvalues are associated with the CFT derivative operators  $\partial\sigma$ ,  $\bar{\partial}\sigma$ , with the phase  $\pm i$  being due to  $\pi/2$  rotation of an operator with spin  $\pm 1$ . Could it be that while the magnitude of derivative operator eigenvalues is not predictable, their phase may be at least approximately predictable for the rotating RG map? Similarly, there are almost imaginary  $\nabla R^\circ$  eigenvalues in the  $\mathbb{Z}_2$ -even sector which may be associated with  $\partial\epsilon$ ,  $\bar{\partial}\epsilon$  and with  $\partial T$ ,  $\bar{\partial}\bar{T}$  (not shown in Table 3 since they belong to the lower part of the spectrum). While we do not quite see how to make this correspondence rigorous for the Jacobian eigenvalues, we will see in [21] that the same pattern holds rigorously for the eigenvalues of the lattice dilatation operator.

*Remark 4.1.* It is interesting to discuss what it would take to approach the critical fixed point tensor with the traditional “shooting” method as closely as  $10^{-9}$  achieved here with the Newton method. To use the shooting method we would need to determine the critical temperature sufficiently precisely and then use a sufficiently large number of iterations to

approach the fixed point. The final accuracy  $\delta_*$  is given in terms of the leading irrelevant  $\mathbb{Z}_2$ -even eigenvalue  $\lambda_{\text{irr}}$  in Eq. (3.8). Using  $\lambda_{\text{irr}} \approx 0.63$  for the non-rotating Gilt-TNR map, we find that  $\delta_* \sim 10^{-9}$  requires  $\Delta t \sim 10^{-23}$ , below the  $\sim 10^{-16}$  machine precision for the double precision arithmetic. (For the rotating Gilt-TNR the required  $\Delta t \sim 10^{-34}$  is much smaller due to  $\lambda_{\text{irr}} \approx 0.78$  being closer to 1.) Thus, to match the precision level of the Newton method with the shooting method would require multiple precision arithmetic, or a tensor RG map with a smaller  $\lambda_{\text{irr}}$ . The theoretical lower limit here is  $\lambda_{\text{irr}} = 0.25$ , corresponding to the  $T\bar{T}$  quasiprimary.

Finally, let us come back to the convergence rate in Fig. 9. We checked numerically that, for all  $s$  in that figure, the convergence rate is compatible with the largest eigenvalue of the Jacobian of the map  $g_\approx$  which is being iterated (as it should be). Here we would like to provide qualitative understanding of why the convergence rate improves with  $s$  and why it eventually saturates, as mentioned above.

From the definition Eq. (2.15) of  $g_\approx$ , its Jacobian at the fixed point is

$$(\nabla g_\approx)(A_*^\circ) = I - J_\approx^{-1}(I - \nabla R^\circ(A_*^\circ)). \quad (4.7)$$

We would like to understand the eigenvalues of this matrix. Recall that  $J_\approx$  is evaluated not at the fixed point but at  $A_{(0)}$  where we start the Newton iterations. Let us consider first an approximation where we neglect this difference:

$$J_\approx \approx I - P_s \nabla R^\circ(A_*^\circ) P_s. \quad (4.8)$$

Then we have to study the largest eigenvalue of the matrix

$$M_s = I - (I - P_s M P_s)^{-1}(I - M), \quad (4.9)$$

where we denoted  $M = \nabla R^\circ(A_*^\circ)$  and where  $P_s$  is the orthogonal projector on the first  $s$  eigenvectors of  $M$ . We have the following

**Lemma 4.1.** *Assume  $M$  is diagonalizable with the eigenvalues  $\lambda_1, \lambda_2, \dots$  arranged in order of decreasing absolute value. Suppose none of the first  $s$  eigenvalues are 1. Then  $M_s$  is diagonalizable with eigenvalues  $0, \dots, 0, \lambda_{s+1}, \lambda_{s+2} \dots$ , where eigenvalue 0 has multiplicity  $s$ .*

The elementary proof is given below. Hence, the predicted convergence rate is  $\lambda_{s+1}$ . For  $s = 3$  this agrees well with Fig. 9, but for larger  $s$  the convergence in Fig. 9 is slower. We assign this discrepancy to the breakdown of the approximation (4.8). We observed that re-evaluating  $J_\approx$  after a few Newton iterations brings the convergence rate closer to the predicted value. In particular, with  $J_\approx$  evaluated at  $A_{(0)}$ , convergence rate saturates around  $s = 54$ , but after re-evaluation convergence keeps improving even for higher  $s$ .

*Proof of Lemma 4.1.* The simple case is when the eigenvectors of  $M$  are orthogonal. Then,  $M_s$  expressed in the basis of eigenvectors is diagonal with

$$0, \dots, 0, \lambda_{s+1}, \lambda_{s+2} \dots \quad (4.10)$$

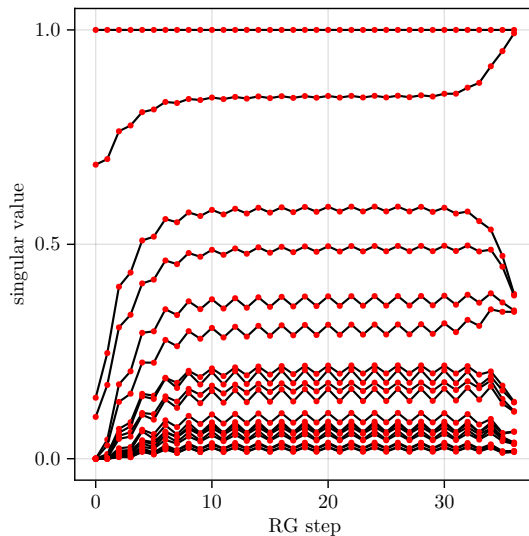


**Figure 12:** Period-2 behavior for the rotating RG map. The figure shows the flow of tensors starting from  $A^{(0)}$  corresponding to the Ising model at the reduced temperature  $t = 1.0000094857$  and with anisotropy  $a = 0.8$ . As in Fig. 4 we plot the 20 largest singular values along the diagonal normalized by the first one.

on the diagonal, proving the lemma. In the general case, we work in the basis obtained by the Gram-Schmidt process from the eigenvectors of  $M$ . In this basis, all the involved matrices are upper-triangular with eigenvalues on the diagonal. In particular  $M_s$  is upper-triangular with (4.10) on the diagonal.  $\square$

## 4.2 Anisotropy: period-2 oscillations

Recall that for the non-rotating RG map the eigenvalues of the Jacobian corresponding to the stress tensor components  $T, \bar{T}$  are 1, and we expect a two-dimensional manifold of fixed points for this map. (A one-dimensional slice of this manifold was studied in Section 3.5.) On the contrary, for the rotating RG map these eigenvalues are  $-1$  and we expect an isolated fixed point embedded in a two-dimensional manifold of period-2 orbits (see Section 2.5). We can see this period-2 behavior by studying the flow of the singular values of  $A$  across the diagonal as we did in Fig. 4 for the non-rotating RG map. We start with an initial  $A$  representing the anisotropic Ising model with  $a = 0.8$ . The flow of the resulting singular values shown in Fig. 12 clearly shows period-2 behavior. Fig. 12 only shows a single value of  $a$ , but we observed that the amplitude of the oscillations increases for larger  $|a - 1|$ . These results confirm our intuition about the structure of the RG flow.

## 5 Summary and open problems

In this paper we showed that the fixed point equation of tensor RG can be solved via the Newton method. This needs a judicious modification of the RG map, to include a  $\pi/2$



rotation of the lattice. The rationale is to avoid eigenvalue 1 deformations of the fixed point, which are problematic for the Newton method. The corresponding eigenvectors are associated with the stress tensor CFT deformations, which have spins  $\ell = \pm 2$ . The  $\theta = \pi/2$  rotation turns their eigenvalues from 1 into  $e^{i\theta\ell} = -1$ , eliminating the problem.

Our numerical tests of this general idea used Gilt-TNR [10], one of several known tensor RG algorithms which implement the disentangling procedure necessary to solve the CDL problem. Working at bond dimension  $\chi = 30$ , the Newton method was shown to converge to the fixed point in the Hilbert-Schmidt distance, with accuracy limited only by roundoff errors. To our knowledge, this is the first time that the Newton method was used to find the critical tensor RG fixed point. Working in double precision arithmetic, we achieved the accuracy  $\delta \sim 10^{-9}$ . This is much better than what was previously achieved with the traditional “shooting” method of recovering the fixed point, where one fine-tunes the relevant temperature perturbation, and removes the irrelevant perturbations by repeated RG steps ( $\delta \sim 10^{-2}$  [19];  $\delta \sim 3 \times 10^{-4}$  [20];  $\delta \sim 5 \times 10^{-5}$  in our Fig. 5).

We would like to conclude by listing several open problems raised by our work:

- In this paper, we used the traditional “shooting” method to get sufficiently close to the fixed point, switching to the Newton method for the final approach. Can one achieve convergence in a larger domain, ideally from the nearest-neighbor 2D Ising tensor at  $T = T_c$ ? One reason why our algorithm converged in a small domain was the use of a fixed approximate Jacobian tensor  $J_{\approx}$ . What about updating this tensor dynamically, as in quasi-Newton methods? Or using the exact Jacobian and evaluating  $[J(A)]^{-1}f(A)$  in (2.13) with an iterative linear system solver?
- In this paper, we relied on Gilt-TNR, with static  $Q$ -choice (Appendix C.2) to ensure differentiability. Can the Newton method be set up for other tensor RG algorithms with disentangling, e.g. for TNR [6], combining them with  $\pi/2$  rotation? Our logic about the rotation getting rid of eigenvalues 1 should be robust. But is TNR differentiable, or even continuous, in spite of the iterative optimization of disentanglers which may be trapped in a local minimum (footnote 25)?
- In this paper we argued on general grounds and provided numerical evidence that the RG map Jacobian at the fixed point has two kinds of eigenvalues. Eigenvalues associated with quasiprimary CFT operators are universal and predictable from CFT, while eigenvalues of derivative operators are not universal and their values cannot be predicted. Our Table 2 contains several eigenvalues which do not agree with any CFT quasiprimary, and we associated their eigenvectors with derivative operators. Is there a test via an explicit computation involving the eigenvectors and the fixed point tensor which can confirm this assignment?
- One somewhat technical issue concerns finding a fully robust gauge-fixing procedure for  $\mathbb{Z}_2$ -odd perturbations of the fixed point, see Appendix D.1.
- Why is gauge fixing with orthogonal gauge transformations enough for a tensor RG map to have a fixed point? This has a satisfactory explanation for maps preserving

reflection symmetry, Appendix D.3, but it is puzzling why this works for many maps used in the literature and in our work, which do not preserve it. In Appendix D.3.2 we tried to explain this conceptual puzzle via an argument appealing to a “phantom” RG map which has not been provided. Can one either exhibit this map, or find another argument which does not postulate its existence?

- Are there practical tensor RG maps which manifestly preserve rotations while solving the CDL problem? One such map of unclear practicality is mentioned in footnote 13 (it acts on a set of three tensors and has a larger than usual associated set of gauge symmetries). Of course, if that map, or any other rotation-invariant map, were available, one could completely circumvent the eigenvalues 1 problem, implementing the Newton method directly within the subspace of rotation-invariant tensors, as discussed in Section 2.4.
- (See Remark 3.1) In this paper we studied the fixed point tensors for a fixed value of  $\chi = 30$  (and sometimes also for  $\chi = 10, 20$ ). This was enough to defend our main points. However, as discussed in Appendix C.3, higher bond dimensions up to  $\chi = 120$  used in [10] may well be accessible, provided that the Jacobian is evaluated via the automatic differentiation instead of finite differences used here. One could then get evidence for or against the hypothesis that the fixed point tensors converge as  $\chi \rightarrow \infty$  to a limiting tensor (which is then necessarily Hilbert-Schmidt). This hypothesis may or may not be true for the Gilt-TNR map, but hopefully there exists a tensor RG map for which it is true.
- Finally, our work is also an important stepping stone towards proving the existence of the critical tensor RG fixed points at the mathematical level of rigor, the program started in [13, 14]. For this dream to be realized, the tensor RG fixed point equation has to be reformulated as a fixed point equation for a map which is a contraction in a neighborhood in an appropriate Banach space of infinite-dimensional tensors. In this paper we have found a numerical realization of a baby version of this program in a finite-dimensional space of truncated tensors.

## Acknowledgments

We thank Glen Evenbly for communications and for his tensor network software and tutorials [30, 38]. We especially thank Clément Delcamp for numerous useful communications and insightful discussions concerning tensor RG algorithms, and for passing to us minimal working versions of the Gilt-TNR algorithm from [10, 32] and of Markus Hauru’s TNR code from [29] (the latter code was not used in this work but it was useful in preliminary stages).

This research was supported in part by the Simons Foundation grant 733758 (Simons Bootstrap Collaboration). This research was supported in part by grant no. NSF PHY-2309135 to the Kavli Institute for Theoretical Physics (KITP).

## A Tensor conventions

### A.1 Tensor RG

Let  $A$  be a four-legged tensor of bond dimension  $\chi$ . Consider a periodic tensor network contraction made out of  $A$  arranged in an  $N \times M$  grid, denoted by

$$Z(A, N \times M), \tag{A.1}$$

and called the partition function of the tensor network. We assume that it represents the partition function of a lattice model of spins with periodic boundary conditions on the  $N \times M$  lattice with short-range interactions, such as Ising or 3-state Potts.<sup>33</sup>

We normalize  $A$  to have  $\|A\| = 1$  where  $\|A\|$  is the Hilbert-Schmidt norm.

Tensor RG maps considered in this paper fall into two categories: 1) non-rotating and 2) involving rotating the network by  $\pi/2$  (“rotating”). Non-rotating tensor RG maps an  $N \times M$  tensor network (A.1) made of  $A$  to an  $N/b \times M/b$  tensor network made of another tensor  $A' = \mathcal{R}(A)$  so that the partition function remains invariant:

$$Z(A, N \times M) = Z(A', N/b \times M/b) \quad (\text{non-rotating}). \tag{A.2}$$

On the other hand, for tensor RG maps with a  $\pi/2$  rotation, invariance of the partition function is written as:

$$Z(A, N \times M) = Z(A', M/b \times N/b) \quad (\text{rotating}). \tag{A.3}$$

There are of course many different tensor RG maps, differing in how  $A'$  is obtained from  $A$ . Some concrete maps were discussed in the main text. Here we keep things general.

In general  $A'$  is not normalized. Multiplying the tensor of which the tensor network is made by a constant factor  $C$  is a relatively minor change, since such a factor can always be factored out from the partition function. It changes the partition function by  $C^N$  where  $N$  is the number of tensors in the network. However this does not change the phase of the microscopic model that the network represents. To discuss phases and fixed points, we have to normalize tensors somehow. We define the normalized RG map by  $R(A) = A'/\|A'\|$ , so that the RG flow happens in the space of unit-norm tensors. We will most often work with  $R(A)$  which is the most important part of the non-normalized RG map  $\mathcal{R}$ . We will sometimes abuse the terminology and refer to  $R$  as the RG map, dropping “normalized”. An RG fixed point for the map  $R$  is a tensor  $A_*$  satisfying  $R(A_*) = A_*$ .

### A.2 Tensor network symmetries

A symmetry transformation of a tensor network is a faithful linear action of a group  $G$  on the space of tensors  $A$ :

$$T_g : A \mapsto A' \quad (g \in G), \tag{A.4}$$

---

<sup>33</sup>Sometimes when the lattice model is translated to a tensor network representation, the spin lattice is rotated by  $\pi/4$  with respect to the tensor network, as in Appendix B. The lattice model then has somewhat unusual periodic boundary conditions. This microscopic detail does not play a role in our paper.

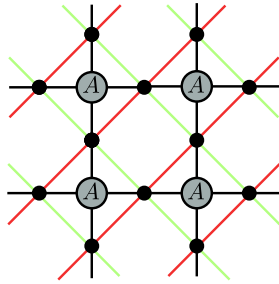


**Figure 13:** The Ising spins (black dots) are located at the midpoints of the bonds in the tensor network. The coupling constants for the Ising model are  $J_y$  for the red bonds and  $J_x$  for the green bonds.

which preserves the partition function of a tensor network built of  $A$ :

$$Z(A, N \times M) = Z(T_g A, N \times M). \quad (\text{A.5})$$

We say that the tensor network built out of a particular tensor  $A_0$  respects this symmetry, if  $A_0$  is invariant under this action:  $T_g A_0 = A_0$  for any  $g \in G$ .

We will consider on-site (global) symmetries and spatial symmetries. An on-site symmetry transformation multiplies tensor  $A$  by matrices on each leg. E.g. an on-site  $\mathbb{Z}_2$  acts as

$$A \mapsto \begin{array}{c} \text{V} \\ \bullet \\ \text{---} \\ \bullet \\ \text{H} \end{array} \quad (\text{A.6})$$

for some matrices  $H, V$  such that  $H^2 = V^2 = I$ .

A spatial symmetry permutes the legs of a tensor and simultaneously multiplies by matrices on each leg. Spatial symmetries mentioned in this paper, on the square lattice, involve a combination of axis reflections and rotations, forming the group  $D_4$  or one of its subgroups  $\mathbb{Z}_2, \mathbb{Z}_2 \times \mathbb{Z}_2, \mathbb{Z}_4$ . E.g. the horizontal reflection acts as:

$$A \mapsto \begin{array}{c} \text{V} \\ \bullet \\ \text{---} \\ \bullet \\ \text{H} \end{array}, \quad (\text{A.7})$$

while rotation by  $\pi/2$  acts as

$$A \mapsto \begin{array}{c} \text{V} \\ \bullet \\ \text{---} \\ \bullet \\ \text{H} \end{array} \quad (\text{A.8})$$

The matrices multiplying the legs must be chosen to get a representation of the spatial symmetry group. Note that they are not in general equal to the identity.

## B Initial tensors for tensor RG evolution

Here we describe the initial tensor for the RG evolution used in our studies, both in the isotropic and anisotropic case. There is more than one way to represent the nearest-neighbor (NN) Ising partition function as the contraction of a tensor network. The method

we use in this paper is the same as used in [3]. In this method the lattice for the Ising model is rotated by  $\pi/4$  with respect to the tensor network. In Fig. 13 the sites for the Ising spins are represented by black dots. The coupling constants on the bonds between these spins are equal to  $J_y$  for the red bonds and  $J_x$  for the green bonds. Note that the Ising spins are located at the midpoints of the bonds in the tensor network. Each leg in the tensor network only takes on the values  $-1, +1$ , corresponding to the values of the Ising spin. The contraction of the tensor network is then equal<sup>34</sup> to the NN Ising partition function if we define the components of the tensor  $A$  by

$$\begin{array}{c}
 \sigma_2 \\
 | \\
 \sigma_1 \text{---} \textcircled{A} \text{---} \sigma_3 \\
 | \\
 \sigma_4
 \end{array} = \exp((J_y\sigma_1\sigma_2 + J_x\sigma_2\sigma_3 + J_y\sigma_3\sigma_4 + J_x\sigma_4\sigma_1)/T). \quad (\text{B.1})$$

The final step in the definition of the initial  $A$  is to apply a gauge transformation that transforms the states  $|+\rangle, |-\rangle$  to the  $\mathbb{Z}_2$  even and odd states given by

$$|0\rangle = \frac{1}{\sqrt{2}}(|+\rangle + |-\rangle), \quad |1\rangle = \frac{1}{\sqrt{2}}(|+\rangle - |-\rangle) \quad (\text{B.2})$$

We define  $a = J_y/J_x$ . For the isotropic case we set  $J_x = J_y = 1$  and then define the reduced temperature by  $t = T/T_c$  so that  $t = 1$  is the critical point. For the anisotropic case we set  $J_y = a, J_x = 1$ , and again let  $t = T/T_c$  where now the critical temperature depends on  $a$ .<sup>35</sup> As in the isotropic case, the critical point is given by  $t = 1$ . Only the parameters  $t$  and  $a$  are used in our discussions of the numerical results. In the numerical results the critical point is not exactly at  $t = 1$  since the bond dimension is finite.

Since the Ising lattice is rotated with respect to the tensor network, in the anisotropic case the initial  $A$  is not invariant under horizontal or vertical reflections. However, it is invariant under the composition of these two reflections.

The initial tensor, which we normalize to have unit Hilbert-Schmidt norm, will be denoted  $A_{\text{NN}}(t, a)$ , or  $A_{\text{NN}}(t)$  if  $a = 1$ .

Another method for representing the Ising partition function as the contraction of a tensor network can be found in [5, 10]. In this approach the Ising lattice is not rotated with respect to the tensor network.

## C More details about Gilt-TNR

We reviewed the general structure of the non-rotating Gilt-TNR algorithm in Section 3.1 and here we will provide some more details.

The basic procedure for choosing  $Q = Q_1$  (see [10, Sec. IV.B] and [19, App. A]) consists of four steps:

<sup>34</sup>Because of the lattice rotation by  $\pi/4$ , the equality requires non-standard periodic boundary conditions on the Ising side, assuming the usual periodic boundary conditions on the tensor network side.

<sup>35</sup>The critical temperature is given implicitly by  $\sinh(2J_y/T_c) \sinh(2J_x/T_c) = 1$ .

$\chi$	tensor bond dimension
$\epsilon_{\text{gilt}}$	soft truncation parameter in (C.1)
$\epsilon_{\text{conv}}$	convergence parameter, see (C.2),(C.4)

**Table 4:** Parameters of Gilt-TNR. Results in this paper used  $\epsilon_{\text{conv}} = 10^{-2}$ .

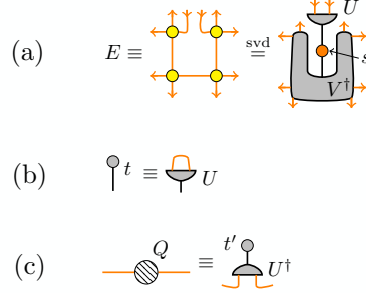


**Figure 14:** Defining the matrix  $Q \equiv Q_1$ : (a) Environment and singular value decomposition; (b) Vector  $t$ ; (c) Matrix  $Q$ . Figures from [19].

- Consider the singular value decomposition of an environment shown in Fig. 14(a), built out of four  $A$  tensors contracted over 3 out of 4 bonds around the plaquette, omitting the bond into which  $Q_1$  will be inserted.
- Form vector  $t$  by contracting two ingoing legs of  $U$ , Fig. 14(b).
- Perform soft truncation of vector  $t$ , defining vector  $t'$  by

$$t'_i = t_i \frac{s_i^2}{s_i^2 + \epsilon_{\text{gilt}}^2}, \quad (\text{C.1})$$

where  $s_i$  are the singular values in Fig. 14(a), and  $\epsilon_{\text{gilt}}$  is one of the three parameters of the Gilt-TNR algorithm (Table 4). Basically, this equation sets to near zero the components of  $t'_i$  corresponding to  $s_i \ll \epsilon_{\text{gilt}}$ .

- Finally define matrix  $Q$  from tensor  $U^\dagger$  and the vector  $t'$  as in Fig. 14(c).

The rationale why this construction is a good way to filter short-range correlations from the plaquette was given in [10].

In practice however the above description is just the first step in an iterative procedure of determining  $Q_1, Q_2, Q_3, Q_4$ . We need two versions of the algorithm, which differ slightly but essentially in how this is implemented:

- “Dynamic  $Q$ -choice”. That’s the one implemented in the original code [32].
- “Static  $Q$ -choice”. This is our modification, essential for ensuring differentiability.

### C.1 Dynamic $Q$ -choice

This is only outlined in [10, Sec. IV.B]. Here we will give a more detailed description, which corresponds to what is actually done in [32]. The dynamic algorithm depends on a parameter  $\epsilon_{\text{conv}}$ , whose default value is  $10^{-2}$ ; it appears in Eq. (C.2) below.

We start by determining  $Q = Q_1$ . To do that, one carries out steps 1-9 for  $k = 0, 1, 2, \dots, k_{\text{max}}$ . Here  $k_{\text{max}}$  is determined dynamically during the run of the algorithm, and it depends on  $\epsilon_{\text{conv}}$  as explained below. Smaller  $\epsilon_{\text{conv}}$  will lead to larger  $k_{\text{max}}$ .

1. Start with the environment  $M^{(k)}$  and the matrix  $Q^{(k)}$ . At the zero step  $M^{(0)} = EE^\dagger$  where  $E$  is in Fig. 14(a) and  $Q^{(0)} = 1$ . By forming this environment out of  $E$ , one avoids having to compute matrix  $V$  in Fig. 14(a), which is not needed in the algorithm.
2. Do approximate SVD of  $Q^{(k)} \approx (Q^{(k)})_L S_{Q^{(k)}} (Q^{(k)})_R$ . Here, all the singular values smaller than  $10^{-3} \epsilon_{\text{gilt}}$  are thrown away. The factor  $10^{-3}$  is hard-coded in [32].
3. Define  $M^{(k+1)}$  by absorbing  $(Q^{(k)})_L \sqrt{S_{Q^{(k)}}}$  and  $\sqrt{S_{Q^{(k)}}} (Q^{(k)})_R$  into  $M^{(k)}$ .
4. By the eigenvalue decomposition of  $M^{(k+1)}$  determine  $U^{(k+1)}$  and  $S^{(k+1)}$ .
5. Form the vector  $t$ .
6. Form the vector  $t'$ .
7. Define  $Q^{(k+1)}$ .
8. Do approximate SVD of  $Q^{(k+1)} \approx Q_L^{(k+1)} S_{Q^{(k+1)}} Q_R^{(k+1)}$ . Again, all the singular values smaller than  $10^{-3} \epsilon_{\text{gilt}}$  are thrown away.
9. Check if

$$\max_i |(S_{Q^{(k+1)}})_i - 1| < \epsilon_{\text{conv}}. \quad (\text{C.2})$$

If this condition does not hold then go to step 1 with  $k \mapsto k + 1$ . Otherwise, we set  $k_{\text{max}} = k$  (this is just to store the total number of carried out iterations) and go to the next step. The rationale for condition (C.2) is that we would like (C.3) below to converge.

10. Define  $Q$  via  $Q^{(0)}, \dots, Q^{(k_{\text{max}})}$  by combining all absorbed pieces in the appropriate order:

$$Q = \prod_{k=0}^{k_{\text{max}}} \left( Q_L^{(k)} \sqrt{S_{Q^{(k)}}} \right) \prod_{k=k_{\text{max}}}^0 \left( \sqrt{S_{Q^{(k)}}} Q_R^{(k)} \right). \quad (\text{C.3})$$

11. Define  $B_1, B_2$  tensors by splitting  $Q$  (using approximate SVD, throwing away eigenvalues  $< 10^{-3} \epsilon_{\text{gilt}}$  again) and absorbing its halves into  $A$ .

This ends the procedure for  $Q_1$ . One then proceeds to do the same for matrices  $Q_3$ ,  $Q_2$ ,  $Q_4$ , in this order.<sup>36</sup> Of course, when we proceed to  $Q_3$ , we use tensors  $B_1$  and  $B_2$  to construct the relevant environments. Once  $Q_3$  is found, we update  $B_1$  and  $B_2$ , and proceed to  $Q_2$ , etc.

Once the  $Q_a$  ( $a = 1, \dots, 4$ ) are constructed, we say that we “completed a lap around the plaquette”. We then check the spectra of  $Q_a = Q_{aL} S_{Q_a} Q_{aR}$  (again truncated SVD) and ask if

$$\max_i |(S_{Q_a})_i - 1| < \epsilon_{\text{conv}}. \quad (\text{C.4})$$

If this condition does not hold for one or more bonds around the plaquette, we are supposed to run the above cycle again for those bonds, redefining yet again matrices  $Q_a$  and tensors  $B_1$ ,  $B_2$ . This will be the second, third, etc lap. In practice one usually needs two laps.

Let us give a couple of examples of how this works in practice. Both examples are for  $\chi = 30$ ,  $\epsilon_{\text{gilt}} = 6 \times 10^{-6}$ ,  $\epsilon_{\text{conv}} = 10^{-2}$ .

1. Applied to  $A^{(n^*)}$  in Table 2, the dynamic algorithm does two laps, with the following number  $k_{\text{max}}$  of  $k$  iterations for  $Q_1, Q_3, Q_2, Q_4$ :

$$\text{Lap 1: (19, 29, 10, 28); \quad Lap 2: (1, 1, 1, 1)}. \quad (\text{C.5})$$

2. Applied to  $A_{(0)}$  in Section 4.1, the dynamic algorithm does two laps, with the following number  $k_{\text{max}}$  of  $k$  iterations for  $Q_1, Q_3, Q_2, Q_4$ :

$$\text{Lap 1: (22, 8, 24, 20); \quad Lap 2: (1, 1, 1, 1)}. \quad (\text{C.6})$$

## C.2 Static $Q$ -choice

In the static algorithm, we do not need the  $\epsilon_{\text{conv}}$  parameter. Instead, we specify the “static instruction”, which includes 1) the number of laps and 2)  $k_{\text{max}}$  values for  $Q_1, Q_3, Q_2, Q_4$  for each lap. The checks of conditions (C.2) and (C.4) of the dynamic algorithm are omitted. The rest of the static algorithm is the same as the dynamic algorithm. This modification ensures that the static algorithm is continuous and differentiable.

The static algorithm is used when we need the RG map to be differentiable, as when the Jacobian is involved. To select a static instruction, we typically run the dynamic algorithm once for a tensor around which we intend to compute the Jacobian.

## C.3 Parameter choices and scaling

In our paper the bond dimension  $\chi$  was varied in the range 10-30, and the parameter  $\epsilon_{\text{gilt}}$  was varied from  $10^{-4}$  for  $\chi = 10$  to  $6 \times 10^{-6}$  for  $\chi = 30$ .

We used the dynamic  $Q$ -choice in calculations which did not need the Jacobian, such as the determinations of the critical temperature via bisection, and Figs. 4, 5, 12. In all dynamic  $Q$ -choice calculations the parameter  $\epsilon_{\text{conv}}$  was fixed to  $10^{-2}$  (the default value of [32]).

---

<sup>36</sup>That  $Q_1$  and  $Q_3$  are chosen before  $Q_2$  and  $Q_4$  is the likely reason for why the horizontal reflection symmetry is broken weaker than the vertical one (footnote 23).



We used the static  $Q$ -choice when computing the Jacobian eigenvalues, and when using the Newton method which needs the map to be differentiable. When computing the Jacobian eigenvalues at  $A^{(n_*)}$  from Table 2, we used the static instruction (C.5) obtained by running once the dynamic algorithm at that tensor. In Section 4.1, we used the dynamic  $Q$ -choice for the RG iterations from  $A^{(0)}$  to  $A^{(n')}$ . Then, we switched to the static  $Q$ -choice with the static instruction (C.6) from the dynamic algorithm at  $A_{(0)} = A^{(n')}$ . We used this static instruction for all subsequent calculations in that section:

- computing the eigenvalue decomposition of  $\nabla R^\circ(A_{(0)})$  which enters  $J_{\approx}$ ;
- running the Newton method and producing Fig. 9;
- computing the Jacobian eigenvalues  $\nabla R^\circ$  at  $A_{(m_*)}$ .

In this paper we limited ourselves to  $\chi \leq 30$  as this was enough to demonstrate our main points regarding the applicability of the Newton method. Ref. [19] also used  $\chi = 30$ . In the future, it would be interesting to carry out our analysis for larger  $\chi$ . (Ref. [10] went up to  $\chi = 120$ .) In the rest of this section, we will discuss how various steps of our algorithms scale with  $\chi$  and which other difficulties may arise when increasing  $\chi$ .

The computational cost of one Gilt-TNR algorithm step scales as  $O(\chi^6)$ . Evaluating the first  $s$  eigenvalues and eigenvectors of  $\nabla R(A)$  at any point  $A$  using Krylov's method scales as  $O(s\chi^6)$ .<sup>37</sup> This operation is required only once when setting up our Newton method with approximate Jacobian, at  $A = A_{(0)}$ . For  $\chi = 30$  and  $s = 9$ , it takes 14 minutes on a laptop. One Newton method step costs  $O(s^2\chi^4 + \chi^6)$ , where  $\chi^6$  comes from the Gilt-TNR step and  $s^2\chi^4$  from applying  $(\mathbb{1} - P_s \nabla R(A_{(0)}) P_s)^{-1}$  to  $A - R(A)$ . For example, for  $\chi = 30$  and  $s = 9$ , a laptop can perform 30 Newton method steps from  $A_{(0)}$ , reaching the approximate fixed point, in 4 minutes (yellow curve in Fig. 9).

The most time-consuming part of our calculations was tuning the critical temperature, which remains necessary as the Newton algorithm may not converge to the critical point from a remote starting tensor. Finding the critical temperature using the bisection method with  $\Delta t = 10^{-10}$  takes around 80 minutes on a laptop.

A potential issue for going to larger  $\chi$  has to do with the error in evaluating the Jacobian via finite differences. As discussed in Appendix E, this error cannot be made arbitrary small due to roundoff errors. For  $\chi = 30$ , the error for an optimal step size  $h$  was quite small (see Fig. 15), at least for derivatives in large eigenvalue directions. However, we observed that the optimal error attainable for the finite difference method increases with  $\chi$ . Extrapolating from  $\chi = 10, 20, 30$ , we suspect that for e.g.  $\chi = 60$  it may reach values which will make the finite difference method unusable. Automatic differentiation techniques [39] famously avoid roundoff errors inherent for the finite difference method. We expect that a rewrite of our code using automatic differentiation would allow to go to higher  $\chi$ .

---

<sup>37</sup>Krylov's method requires  $O(s)$  evaluations of directional derivatives  $\nabla R^\circ.v$ , each of which takes  $O(\chi^6)$  with our finite difference approximation method.

### C.4 Gilt-HOTRG [19]

In this section we will describe the algorithm used in Ref. [19, 40], which somewhat differs from Gilt-TNR used in [10] and our work. We will refer to it as Gilt-HOTRG. Having this description is useful to understand and appreciate some details of the results of Ref. [19], such as for example the fact that their linearized RG map coincides with the lattice dilatation operator and hence its eigenvalues agree with (exponentiated) CFT scaling dimensions even for descendants [21].

As the name suggests, Gilt-HOTRG [19] combines Gilt with HOTRG [5], i.e. it uses Gilt to filter local correlations, and HOTRG for coarse-graining, while Gilt-TNR uses TRG for coarse-graining. The main equation which defines their RG transformed tensor in terms of the original tensor is (figure from [19], Eq. (31)):

(C.7)

Let us explain this equation further. As a first step, one chooses Gilt matrices  $Q_B$  and  $Q_A$ , applying the Gilt procedure to horizontal links of a subset of plaquettes (figure from [19], Fig. 11)):

(C.8)

As one can see in (C.8), matrices  $Q_B$  and  $Q_A$  are then SVD-decomposed, and their halves are absorbed into  $A$  (this step breaks reflection symmetry since in general  $Q_{Br} \neq (Q_{Bl})^t$ ,  $Q_{Ar} \neq (Q_{Al})^t$ ). One then performs HOTRG coarse-graining in the vertical direction, using isometries  $w, w^\dagger$  in (C.7) (see also [19], Eq. (A6)).

As a second step, the whole procedure is repeated in the horizontal direction. The final result is an RG map which reduces the lattice size by factor 2 in both directions.

Ref. [19] do not mention if they use iterative optimization of Gilt matrices.

Gilt-HOTRG is a non-rotating RG map, so it has eigenvalues 1 around the fixed point. Like Gilt-TNR, it can be accompanied by a rotation, turning eigenvalues 1 to  $-1$  and making the Newton method applicable.

## D Gauge fixing

As mentioned in Section 3.2, to see that the tensors  $A^{(n)}$  converge to a fixed point, we need to apply after each Gilt-TNR step an appropriately chosen gauge transformation. Tensors related by a gauge transformation are physically equivalent as they yield the same partition function. We need to choose a unique tensor from each gauge equivalence class to discuss the fixed point tensor. This can be done by employing a gauge fixing procedure.

A general gauge transformation preserving the partition function would consist in multiplying the tensor on horizontal legs with matrices  $G_h^{-1}$  and  $G_h$  where  $G_h$  is an invertible  $\chi \times \chi$  matrix, and similarly on the vertical legs with  $G_v^{-1}$  and  $G_v$ . In this work, we used a restricted class of gauge transformation where  $G_v, G_h$  are orthogonal matrices.

Why are orthogonal gauge transformations enough? This may be expected by looking at the trajectories of singular values along the diagonal, which show plateaux (Fig. 4). Indeed, singular values are invariant under orthogonal gauge transformations, see Eq. (3.6), while they would not be invariant under more general gauge transformations with invertible matrices. For further rationale see Appendix D.3.

For orthogonal gauge transformations we have  $G_h^{-1} = G_h^T$ ,  $G_v^{-1} = G_v^T$ . Graphically such a gauge transformation acts on a four-legged tensor  $A$  of bond dimension  $\chi$  as follows:

$$A \text{ (with legs)} \mapsto A_G = \begin{array}{c} G_v \\ \text{---} \bullet \text{---} \\ G_h \end{array}, \quad (\text{D.1})$$

where  $G_v, G_h \in O(\chi)$ .

“Gauge fixing” means that we will apply the gauge transformation (D.1) with some appropriately chosen  $G_v, G_h$ . Our gauge fixing procedure involves continuous gauge fixing followed by discrete gauge fixing. Continuous gauge fixing is done as follows. Consider the following two contractions of two copies of  $A$ , called environments:

$$(\text{env}_v(A))_{ij} = \begin{array}{c} i \quad j \\ \text{---} \bullet \quad \bullet \text{---} \\ \text{---} \bullet \quad \bullet \text{---} \\ \text{---} \bullet \quad \bullet \text{---} \\ j \quad i \end{array}, \quad (\text{env}_h(A))_{ij} = \begin{array}{c} i \\ \text{---} \bullet \\ \text{---} \bullet \\ \text{---} \bullet \\ j \end{array}. \quad (\text{D.2})$$

The contractions in (D.2) are chosen in such a way that both  $\text{env}_v(A)$  and  $\text{env}_h(A)$  are symmetric and can be diagonalized by orthogonal matrices. We choose  $G_v$  and  $G_h$  that diagonalize these environments. Then we perform the gauge transformation (D.1). The tensor  $A_G$  is the result of continuous gauge fixing.

There is some ambiguity in the choice of  $G_v$  and  $G_h$ . If the spectra of  $\text{env}_v(A)$  and  $\text{env}_h(A)$  are nondegenerate, as is generically true, then this ambiguity reduces to multiplying  $G_v \rightarrow G_v S_v$  and  $G_h \rightarrow G_h S_h$  where  $S_v$  and  $S_h$  are diagonal matrices with  $\pm 1$  on the diagonal. In terms of  $A_G$ , this amounts to applying an additional gauge transformation:

$$A_G \text{ (with legs)} \mapsto A_{GS} = \begin{array}{c} S_v \\ \text{---} \bullet \text{---} \\ S_h \end{array}, \quad (\text{D.3})$$

Discrete gauge fixing amounts to choosing the matrices  $S_v$  and  $S_h$  appropriately. The tensor  $A_{GS}$  is the final result of our gauge fixing procedure.

Note that there are some replacements of  $S_v, S_h$  which leave  $A_{GS}$  invariant:

- $S_v \mapsto -S_v$ ;
- $S_h \mapsto -S_h$ ;
- the simultaneous replacement  $S_v, S_h \mapsto VS_v, HS_h$  provided that, as is the case for us, the tensor  $A_G$  enjoys a  $\mathbb{Z}_2$  symmetry

$$\text{---} \circ \text{---} = \text{---} \circ \begin{matrix} \color{red}{\bullet} V \\ \color{green}{\bullet} \color{red}{\bullet} \\ \color{red}{\bullet} H \end{matrix} \text{---} \quad (\text{D.4})$$

with  $H, V$  diagonal matrices with  $\pm 1$  on the diagonal (see Eq. (A.6)).

We will perform discrete gauge fixing by imposing the following gauge fixing condition on the tensor  $A_{GS}$ :

$$(A_{GS})_{ijkl} > 0, \quad \forall (i, j, k, l) \in I_+. \quad (\text{D.5})$$

for an appropriately chosen set of tensor components  $I_+ \subset \{1, \dots, \chi\}^4$ . In words, this says that after the discrete gauge transformation, a certain subset of (nonzero) tensor components should be positive. Equivalently, Eq. (D.5) can be written as

$$(S_v)_i (S_h)_j (S_v)_k (S_h)_l = \text{sign}((A_G)_{ijkl}), \quad \forall (i, j, k, l) \in I_+, \quad (\text{D.6})$$

where we introduced a shorthand notation  $(S_v)_i$  for  $(S_v)_{ii}$ .

The set  $I_+$  should be not too large (because otherwise (D.6) will not have a solution) and not too small (because otherwise (D.6) will have multiple solutions and the gauge fixing will not be complete). In other words,  $I_+$  should be such that  $S_v, S_h$  satisfying (D.6) are unique (up to the above-mentioned replacements which do not change  $A_{GS}$ ).

How do we choose a suitable  $I_+$  and solve (D.6)? Let  $I_{\neq 0}$  be the set of all components such that  $(A_G)_{ijkl} \neq 0$  for all  $(i, j, k, l) \in I_{\neq 0}$ . Consider *all* equations of the form

$$(S_v)_i (S_h)_j (S_v)_k (S_h)_l = \text{sign}((A_G)_{ijkl}), \quad (\text{D.7})$$

where  $(i, j, k, l) \in I_{\neq 0}$ . Let us parametrize

$$(S_v)_i = (-1)^{v_i}, \quad (S_h)_i = (-1)^{h_i}, \quad \text{sign}((A_G)_{ijkl}) = (-1)^{a_{ijkl}}, \quad (\text{D.8})$$

where  $h_i, v_i, a_{ijkl} \in \{0, 1\}$ . Then we rewrite equations (D.7) as linear equations in modular arithmetic:

$$v_i + h_j + v_k + h_l = a_{ijkl} \pmod{2}. \quad (\text{D.9})$$

Note that the number of these equations is much higher than the number of unknowns, thus we cannot hope to solve all of them (in other words, we cannot hope to find a discrete gauge transformation that makes *all* nonzero elements of  $A_{GS}$  positive). Instead, we will choose a specific subset  $I_+ \subset I_{\neq 0}$  and solve the corresponding subset of equations. To

choose  $I_+$ , we first order equations (D.9) in the order of decreasing  $|(A_G)_{ijkl}|$ . Then, we form the matrix  $M$  so that (ordered) (D.9) can be written as

$$M\vec{x} = \vec{a}, \tag{D.10}$$

where  $\vec{x}$  is the vector of  $2\chi$  unknowns which combines  $h_i$ 's and  $v_i$ 's. Next, we perform Gaussian elimination on  $M$  to identify a maximal independent set of rows, starting with row 1 and then trying subsequent rows one by one and adding them to the set if they are linearly independent from the previously added rows, until no more rows can be added. The resulting set of linearly independent rows is what gives us the set  $I_+$ . We find that the size of  $I_+$  is, as expected,  $2\chi - 3$ , corresponding to  $2\chi$  unknowns minus 3 transformations which were discussed above and which determine the kernel of  $M$ .

Note that the choice of  $I_+$  described so far depends only on the ordering of equations (D.9) in the order of decreasing  $|(A_G)_{ijkl}|$  that we chose. Now we take system Eq. (D.10), restrict it to rows  $I_+$ , and solve for  $\vec{x}$  in terms of  $\vec{a}$ . The solution is not unique but as discussed different solutions are equivalent since they give the same  $A_{GS}$ . In practice, for this last step we use a Julia [34, 35] package `AbstractAlgebra.jl` [41, 42], which includes a linear solver for finite fields.<sup>38</sup> We use this solution to fix the discrete gauge.

From the described procedure, it can be seen that  $I_+$  as defined above will remain constant in a small neighborhood  $U_1$  of  $A$  in which the ordering of the elements  $|(A_G)_{ijkl}|$  which enter into its definition does not change. This is a good feature. Indeed, if  $I_+$  changed as  $A$  varied, this could lead to discontinuities in the RG map. We cannot allow such discontinuities: we want our RG map to be continuous and even differentiable. In our final algorithm, we enforce  $A$ -independence of  $I_+$  in an even larger neighborhood  $U_2 \supset U_1$  by first computing  $I_+$  for a tensor  $A_{\approx}$  approximating the critical fixed point tensor, and then using exactly the same  $I_+$  everywhere in  $U_2$ . The size of  $U_2$  is determined by the condition that no tensor element  $|(A_G)_{ijkl}|$  with  $(i, j, k, l) \in I_+$  vanishes in  $U_2$ .

### D.1 Comment about gauge fixing for $\mathbb{Z}_2$ -odd perturbations

The previous discussion solves the gauge-fixing problem with the  $\mathbb{Z}_2$ -even subspace to which the fixed point tensor  $A_*$  belongs, and within which the RG evolution converging to  $A_*$  takes place. For a tensor  $A$  not belonging to the  $\mathbb{Z}_2$ -even subspace,  $R(A)$  as described up to now would be computed up to a  $\mathbb{Z}_2$  symmetry transformation. It is important to fix this ambiguity consistently, to get a differentiable map in a neighborhood of a fixed point.<sup>39</sup> In our algorithm, this is fixed as follows. The potential source of ambiguous signs is the singular value decomposition (SVD) operation  $M = U\Lambda V$  since multiplying row  $i$  of  $U$  by a sign  $s_i$  while simultaneously multiplying column  $i$  of  $V$  by the same sign gives an equally valid SVD. It is hard to control how these signs are chosen in a built-in SVD function. Instead, our algorithm uses a custom-made SVD function which, after calling the built-in

<sup>38</sup>The linear solver returns one solution and, optionally, the kernel of the matrix, corresponding in our case to vectors that realize symmetries discussed before Eq. (D.4).

<sup>39</sup>In practice, this need arises when evaluating the Jacobian eigenvalues around the fixed point in the  $\mathbb{Z}_2$ -odd sector. This requires computing  $R(A_* + \delta A)$  for small  $\mathbb{Z}_2$ -odd perturbations  $\delta A$ .

SVD, applies the above transformation with

$$s_i = \text{sign}\left(\sum_j w_j U_{ij}\right), \quad (\text{D.11})$$

where  $w_j$  are some chosen fixed weights, e.g.  $w_j = 1$ .

This simple trick, combined with the gauge-fixing procedures described above, is sufficient to get a differentiable map in a neighborhood of  $A_*$ , including the  $\mathbb{Z}_2$ -odd directions with some rare exceptions. When one considers a family of problems, like in Section 3.5, where we varied the anisotropy parameter  $a$ , this method fails for a few parameter values. The method can also fail for a few values of  $a$  when one varies the step size,  $s$ , in the numerical differentiation. We conjecture this happens because at some step of the algorithm a row of  $U$  occurs whose elements nearly sum to zero, so that (D.11) becomes numerically ill defined. In some but not all cases this problem can be solved by using a different weight vector in (D.11), such as e.g.  $w_j = 1/(1+j)$ . Further work is needed to fully understand this problem.

## D.2 Relation with the approach of Ref. [19]

Let us now discuss how our gauge fixing procedure relates to the procedure used in Ref. [19]. Their RG map, Gilt-HOTRG, was reviewed in Appendix C.4 (without gauge fixing step). It can be seen from the definition of Gilt-HOTRG that if the tensor  $A$  is acted upon by an orthogonal gauge transformation, this has no effect on  $A'$ . This is because various unitary matrices which enter into SVD decompositions and the HOTRG step transform in such a way that the final result remains unchanged (see [19, Appendix B] for a discussion). Based on this observation, Ref. [19] observe that there is no need to perform continuous gauge fixing in their algorithm.<sup>40</sup>

Of course, discrete gauge fixing is essential for Ref. [19] as it is for us. Regarding discrete gauge fixing, there are two main differences between our procedure and the procedure in Ref. [19]. The first one is that instead of the search of  $I_+$ , Ref. [19] makes a particular choice of this subset. While they do not provide exhaustive details, it appears to us that they pick  $I_+$  to contain elements of the form  $(i^+, 1^+, 1^+, 1^+)$ ,  $(1^+, i^+, 1^+, 1^+)$ ,  $(i^-, 1^-, 1^+, 1^+)$ ,  $(1^-, i^-, 1^+, 1^+)$ , where the superscript refers to the  $\mathbb{Z}_2$  quantum number. The second difference is that instead of absolute gauge fixing condition (D.5), Ref. [19] imposes a relative condition:

$$\text{sign}((A'_S)_{ijkl}) = \text{sign}(A_{ijkl}), \quad \forall (i, j, k, l) \in I_+. \quad (\text{D.12})$$

The choice of  $I_+$  as above allows to solve Eq. (D.12) easily (so no need to solve a system of linear equations in modular arithmetic, as in our algorithm). Specifically, we can fix

---

<sup>40</sup>As a matter of fact, this observation also applies to Gilt-TNR used to our work. In fact we have checked that the fixed point is reached even if the continuous gauge fixing step is omitted in our algorithm. Nevertheless, we decided to keep the continuous gauge-fixing step, since it is not expensive. Also, having this step prompted us to reflect more deeply why the orthogonal gauge fixing is actually sufficient in our algorithm, Appendix D.3.

$(S_h)_{1+} = (S_v)_{1+} = (S_v)_{1-} = 1$  using the symmetries discussed after Eq. (D.3). Then, the solution of Eq. (D.12) is

$$\begin{aligned}
(S_h)_{i+} &= \text{sign}(A'_{i+1+1+1+})\text{sign}(A_{i+1+1+1+}), \\
(S_v)_{i+} &= \text{sign}(A'_{1+i+1+1+})\text{sign}(A_{1+i+1+1+}), \\
(S_h)_{i-} &= \text{sign}(A'_{i-1-1+1+})\text{sign}(A_{i-1-1+1+}), \\
(S_v)_{i-} &= \text{sign}(A'_{1-i-1+1+})\text{sign}(A_{1-i-1+1+})(S_h)_{1-}.
\end{aligned}
\tag{D.13}$$

In our opinion, our discrete gauge fixing method is better protected from vanishing tensor elements in  $I_+$  than the procedure in Ref. [19]. In practice, however, both procedures work well and allow one to demonstrate the convergence of the RG flow to the critical tensor (see Fig. 5 and Ref. [19, Fig. 9]).

### D.3 Why is orthogonal gauge fixing enough?

We would like to reflect here, non-rigorously, on why gauge fixing via orthogonal gauge transformations was enough to get, in Sections 3 and 4, RG maps having fixed points.

An RG map is designed to preserve the partition function. When an RG evolution starts from an initial tensor corresponding to the critical temperature, it is reasonable to expect that, with a bit of care and luck,<sup>41</sup> a fixed-point tensor will be reached, as long as an appropriate gauge fixing is incorporated. However, we may expect that a gauge fixing with general invertible matrices may be needed, as this is the most general transformation of tensors preserving the partition function. We know of only one work [20] which used such a general gauge fixing, by going to the Minimal Canonical Form [37]. The works which studied the singular values along the diagonal without doing explicit gauge fixing (e.g. [10, 33]) also provide evidence that orthogonal gauge fixing is enough, since general gauge fixing does not leave these singular values invariant. So while general gauge fixing may be useful, it does not appear indispensable.

Let us assume that we are given an RG map  $R$  which has a fixed point tensor  $A_*$ , up to gauge fixing with general invertible matrices:

$$R(A_*) = \begin{array}{c} \text{---} G_v^{-1} \\ \text{---} G_h^{-1} A_* \\ \text{---} G_h \\ \text{---} G_v \end{array} . \tag{D.14}$$

(So that if we redefine  $R$  by including gauge fixing into it,  $A_*$  would become a fixed point.)

Our strategy will be as follows. First, we will discuss tensors and RG maps satisfying some additional assumptions, namely the presence of reflection symmetry. Under those assumptions, we will show that if (D.14) holds, then a similar equation holds with orthogonal gauge fixing matrices, i.e. orthogonal gauge fixing is enough. Then we will consider the case of weakly broken reflection symmetry, as is the case for the maps in Sections 3 and 4.

<sup>41</sup>By care we mean e.g. the need to solve the CDL problem. By luck we mean e.g. that it is hard to a priori exclude such situations as cycles of finite length. For example, discrete dynamical systems are known to generically undergo period-doubling bifurcations.

### D.3.1 With reflection symmetry

Suppose that the following conditions hold in addition to (D.14):

- Tensor  $A_*$  respects horizontal reflection symmetry in the form:

$$\begin{array}{c} A_* \\ \text{---} \circ \text{---} \\ \text{---} \end{array} = \begin{array}{c} T_v \\ | \\ A_* \\ \text{---} \circ \text{---} \\ | \\ T_v \end{array}, \quad (\text{D.15})$$

where  $T_v$  is a diagonal matrix with  $\pm 1$  on the diagonal. Note that this is not the most general form of reflection symmetry compared to (A.7) as we don't include matrices on the horizontal legs.

- Tensor  $A_*$  also respects vertical reflection symmetry in the form of equation analogous to (D.15) where crossing of vertical legs is equivalent to multiplying horizontal legs by  $T_h$ .
- Tensor  $R(A_*)$  also respects both horizontal and vertical reflection symmetry, in the form of equations like (D.15) (with  $A_*$  replaced by  $R(A_*)$ ) and of its vertical analogue, and with exactly the same  $T_v, T_h$ .
- $G_v$  and  $G_h$  in (D.14) commute with  $T_v$  and  $T_h$ , respectively. This is very natural. The eigenvalues of  $T_v$  and  $T_h$  have the meaning of the reflection quantum numbers of the basis elements of the vertical and horizontal bond Hilbert spaces. We expect that gauge transformations may mix only vectors having the same quantum numbers (both reflections and  $\mathbb{Z}_2$ ). For reflections, this implies  $[G_v, T_v] = [G_h, T_h] = 0$ .

Under the above assumptions, we can prove that an analogue of (D.14) holds with orthogonal gauge fixing matrices.

*Proof.* Consider the polar decomposition of  $G_h, G_v$  of the form

$$G_h = P_h R_h, \quad G_v = P_v R_v, \quad (\text{D.16})$$

where  $R_h, R_v$  are orthogonal and  $P_h, P_v$  are symmetric positive matrices. Note that since in this paper we work with real tensors, we assume that  $G_h, G_v$  are real.

Now consider the following string of equations:

$$\begin{array}{c} T_v \\ | \\ A_* \\ \text{---} \circ \text{---} \\ | \\ G_v^{-1} \\ | \\ T_v \end{array} \begin{array}{c} G_v \\ | \\ P_h R_h \end{array} \stackrel{(4)}{=} \begin{array}{c} T_v \\ | \\ R(A_*) \\ \text{---} \circ \text{---} \\ | \\ T_v \end{array} \stackrel{(3)}{=} \begin{array}{c} \text{---} \circ \text{---} \\ | \\ R(A_*) \\ \text{---} \circ \text{---} \\ | \\ \text{---} \end{array} \stackrel{(1)}{=} \begin{array}{c} G_v \\ | \\ A_* \\ \text{---} \circ \text{---} \\ | \\ P_h R_h \\ | \\ G_v^{-1} \end{array} \stackrel{(2)}{=} \begin{array}{c} G_v \\ | \\ A_* \\ \text{---} \circ \text{---} \\ | \\ T_v \\ | \\ G_v^{-1} \end{array} \begin{array}{c} P_h^{-1} R_h \end{array}. \quad (\text{D.17})$$

We read it from the center towards the sides. In (1) we used (D.14) replacing  $G_h = P_h R_h$ . In (2) we used reflection symmetry of  $A_*$ . In (3) we used reflection symmetry of  $R(A_*)$ . In (4) we used (D.14). Now compare the rightmost and leftmost term in (D.17). Using that



$[G_v, T_v] = 0$  on the vertical legs, and multiplying by  $P_h^{-1}R_h^{-T}$  and  $R_h^{-1}P_h$  on the horizontal legs, we obtain:

$$\begin{array}{c}
 | \\
 A_* \\
 \bullet \\
 P_h^{-2} \text{---} \text{---} P_h^2 \\
 |
 \end{array}
 =
 \begin{array}{c}
 | \\
 A_* \\
 \bullet \\
 \text{---} \text{---} \\
 |
 \end{array}
 .
 \quad (D.18)$$

This equation means that  $A_*$  commutes with  $P_h^2$ , when multiplied on horizontal legs, for any values of vertical indices. By standard arguments it then also commutes with  $f(P_h^2)$  for any  $f$ . In particular choosing  $f(x) = \sqrt{x}$  we obtain that  $A_*$  commutes with  $P_h$ .

Repeating the above argument in the vertical direction we obtain that  $A_*$  also commutes with  $P_v$  when multiplied on vertical legs. Combining the two properties, we obtain that the r.h.s. of (D.14) in fact equals

$$\begin{array}{c}
 R_v \\
 | \\
 A_* \\
 \bullet \\
 R_h^T \text{---} \text{---} R_h \\
 | \\
 R_v^T
 \end{array}
 .
 \quad (D.19)$$

Thus we obtain that  $R(A_*)$  equals  $A_*$  up to an orthogonal gauge transformation.  $\square$

*Remark D.1.* That orthogonal gauge fixing should be enough to get a fixed point for RG maps preserving reflection symmetry was stated without proof in e.g. [12, 22]. We don't know a place where this statement was proven before our work.

### D.3.2 Without reflection symmetry

The above result would be good for us if our RG maps preserved reflections. Unfortunately they do not. They do not even preserve reflections in a weaker form (A.7) with matrices on both horizontal and vertical legs. Breaking of reflections occurs for two reasons. First, the matrices  $Q_1, Q_2, Q_3, Q_4$  are chosen consecutively in (3.1). Second, when these matrices are SVD-decomposed in the r.h.s. of (3.1), the left and the right parts of the decompositions are not transposes of each other, unless the  $Q_i$ 's are positive definite, which is not generally the case.

We note in passing that the RG map in [10] (which is the same as our RG map without rotation) and the RG maps in [19] also break reflections.<sup>42</sup> Why then is orthogonal gauge fixing enough for all these maps, including ours, to exhibit a fixed point?

We would like to advance here one possible reason, which has to do with our maps breaking reflections only weakly. Consider first the rotating RG map from Section 4. It has a fixed point attainable by the Newton method. If the map preserved reflections, the existence of a fixed point with orthogonal gauge fixing would not be surprising given the result from the previous subsection. We know that the reflections are broken, but rather weakly, as can be seen from the fact that the fixed point tensor elements in Table 2, column 3, which are related by reflections do differ, but not too much. Given this, we may speculate that our map is perhaps close to some ‘‘phantom’’ RG map which does preserve reflections (and hence has a fixed point with orthogonal gauge fixing). The existence of a

<sup>42</sup>We believe the statement to the contrary below Eq. (B5b) in [19] to be incorrect.

fixed point for our map would then be natural, given that the Jacobians of our map and of the “phantom” RG map are close, and that it is the Jacobian which enters into the Newton method. The non-rigorous part of this argument is that we haven’t proved the existence of the “phantom” RG map.

As to the RG map without rotation, we can try to think along the same lines (with Table 2, column 2 instead of column 3), up to one further subtlety. Namely, as discussed many times in this paper, the map without rotation has eigenvalues 1 due to the existence of aspect-ratio changing deformations of the fixed point. Consider the set of critical tensors corresponding to aspect ratio 1 (rotation symmetry). These are the tensors for which the anisotropy ellipse is a circle. It is a nonlinear submanifold of the space of all tensors, over which we have little control apart from its existence. The RG map preserves the criticality and the aspect ratio, hence acts within this submanifold (see Section 2.4). Within the submanifold there are no eigenvalues 1, and the above argument may apply.

We stress again that the just given arguments are highly non-rigorous. Unfortunately we don’t have better arguments for the moment.

## E Gilt-TNR differentiability

Let  $R$  be the Gilt-TNR map described in Section 3.1 followed by the gauge fixing procedure from Appendix D. In this appendix, we will explore the smoothness properties of this RG map. In particular, we will provide evidence that the map  $R$  is thrice differentiable in a neighborhood of the critical fixed point tensor  $A_*$ .

Let  $A$  be an approximation of  $A_*$  and  $v$  be a four-legged tensor with the same bond dimension. We can try to evaluate the derivative of  $R$  at  $A$  in the direction  $v$  using the symmetric finite difference approximation. This approximation depends on the step size  $h$  and is given by Eq. (3.11) which we copy here

$$D_s = \frac{R(A + hv) - R(A - hv)}{2h}. \quad (\text{E.1})$$

Without loss of generality, we assume that  $v$  is unit-normalized.

Standard considerations[43, Sec. 5.7] suggest that we will have

$$D_s = (\nabla R).v + \epsilon_t + \epsilon_r, \quad (\text{E.2})$$

where  $\epsilon_t$  is the truncation error (from truncating the Taylor series), and  $\epsilon_r$  is the roundoff error due to accumulated numerical errors in the evaluation of  $R(A \pm sv)$ . For  $R$  thrice differentiable in a neighborhood of  $A_*$ , we may Taylor-expand  $R(A \pm hv)$ , up to  $h^3$  terms given the differentiability assumption. The  $O(h^0)$  and  $O(h^2)$  terms canceling when using the symmetric difference, we obtain  $\epsilon_t \sim h^2$ . On the other hand  $\epsilon_r$  can be estimated as  $\epsilon_r \sim \epsilon_R/h$  where  $\epsilon_R$  is the roundoff error in evaluation of  $R$ . We thus expect

$$D_h = (\nabla R)(A).v + O(h^2) + O(\epsilon_R/h). \quad (\text{E.3})$$

Note that the  $O(h^2)$  truncation error is expected to scale smoothly with  $h$ , with overall size which depends on the direction of  $v$ , while the  $O(\epsilon_R/h)$  roundoff error is expected to be random but of a magnitude which is largely  $v$  independent.

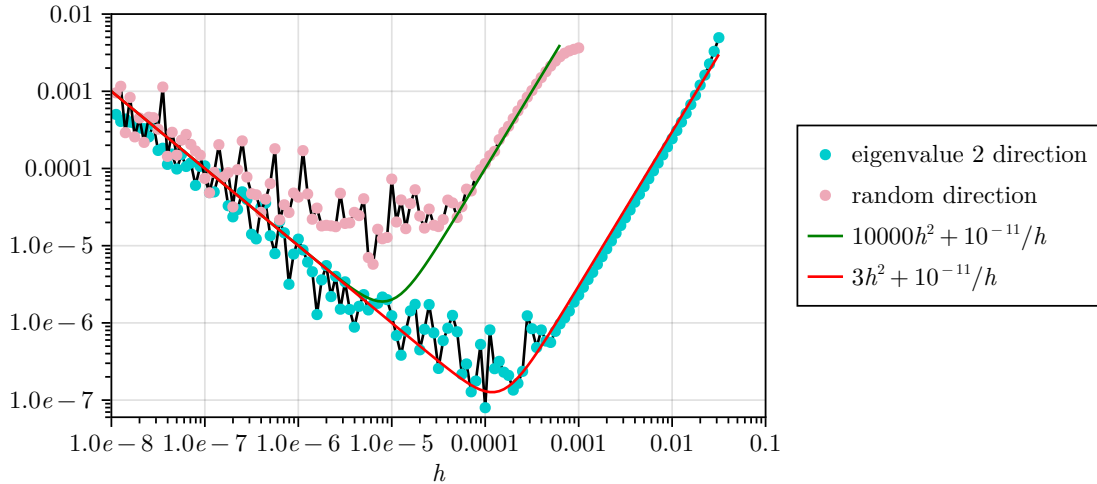


**Figure 15:** The result of the differentiability test for Gilt-TNR at the approximate fixed point for  $\chi = 30$  given in Table 2. The green and red lines illustrate the qualitative behavior of asymptotics and serve to guide the eye. The coefficients for the  $h^2$  and  $1/h$  terms in both lines have been fixed manually to get a visually reasonable agreement, and not as a result of a fit. The  $10^{-11}$  coefficient of the  $1/h$  term gives an idea of the roundoff error of Gilt-TNR.

Our first goal is to test this equation. We will do it by computing  $D_h$  for a discrete sequence of values of  $h$ ,  $h_q \rightarrow 0$  geometrically, and monitoring the differences  $D_{h_q} - D_{h_{q+1}}$ . Fig. 15 shows the result of this test for Gilt-TNR parameters:  $\chi = 30$ ,  $\epsilon_{\text{gilt}} = 6 \times 10^{-6}$ , for  $A = A^{(n^*)}$  from Table 2, and for two choices of a unit-normalized direction  $v$ . The first direction is along the eigenvector of  $\nabla R$  with the largest  $\mathbb{Z}_2$ -even eigenvalue,  $\lambda \approx 2$ .<sup>43</sup> The second direction is a random tensor. (We repeated this test for several random  $v$ 's, with similar results.) On the vertical axis of Fig. 15 we show the difference  $\|D_{h_q} - D_{h_{q+1}}\|$  as a function of  $h_q = 10^{-3-0.05q}$ .

Let us discuss what we observe in Fig. 15. Consider first the test result for the random direction. In this case,  $D_h$  converges as  $O(h^2)$  for  $7 \times 10^{-5} < h < 5 \times 10^{-4}$ . For  $h > 5 \times 10^{-4}$ , the points deviate from  $O(h^2)$ , indicating that higher-order terms become significant. For  $h < 7 \times 10^{-5}$ , the points exhibit chaotic behavior until around  $h = 10^{-6}$ , where they start aligning with the  $O(\epsilon_R/h)$  line as predicted. The poor agreement of the test result with Eq. (E.3) for  $10^{-6} < h < 7 \times 10^{-5}$  may be due to the fact that the random vector  $v$  has a large overlap with the lower part of the  $\nabla R$  spectrum, which is perhaps more sensitive to

<sup>43</sup>We obtained the eigenvector using Krylov's method. For this, we approximated  $\nabla R.v$  using finite difference formula Eq. (E.1) with  $h = 10^{-4}$ .

rounding errors. As to the test result for the eigenvalue 2 direction, it agrees with Eq. (E.3) very well over the full range, except for  $h > 0.03$ , where points start deviating from the  $O(h^2)$  line, which again must be due to higher-order corrections.

We consider these results to agree well with Eq. (E.3), providing evidence that our RG map is at least thrice differentiable near the fixed point. Note that the coefficients of the  $1/h$  chaotic behavior at small  $h$  are roughly similar in Fig. 15 for both directions, in agreement with Eq. (E.3) for  $\epsilon_R \sim 10^{-11}$ . On the other hand the coefficients of the  $h^2$  truncation error are vastly different, which suggests that the third derivative along a random direction is much larger than along a typical direction corresponding to low-lying eigenvalues.

We also used Fig. 15 to optimize the choice of  $s$  in (E.1). We chose  $h = 10^{-4}$  for our computations, because: 1) This is very close to the optimal spot for the eigenvalue 2 direction, where  $O(h^2) + O(\epsilon_R/h)$  error is minimal; 2) The derivative in the random direction has effectively converged at  $h = 10^{-4}$ , and rounding errors have not yet spoiled the result. Based solely on the result for the random direction, a better choice could appear to be  $h \approx 6 \times 10^{-5}$  where, despite the noise,  $\|D_{h_q} - D_{h_{q+1}}\|$  takes the smallest values. However, we believe  $h = 10^{-4}$  is more appropriate as we are primarily concerned with derivatives in the directions of large eigenvalue vectors of  $\nabla R$ .

## References

- [1] M. Levin and C. P. Nave, “Tensor renormalization group approach to 2D classical lattice models,” *Phys. Rev. Lett.* **99** no. 12, (2007) 120601, [arXiv:cond-mat/0611687](#).
- [2] Z. Y. Xie, H. C. Jiang, Q. N. Chen, Z. Y. Weng, and T. Xiang, “Second Renormalization of Tensor-Network States,” *Phys. Rev. Lett.* **103** no. 16, (2009) 160601, [arXiv:0809.0182 \[cond-mat.str-el\]](#).
- [3] Z.-C. Gu and X.-G. Wen, “Tensor-entanglement-filtering renormalization approach and symmetry-protected topological order,” *Phys. Rev. B* **80** no. 15, (2009) 155131, [arXiv:0903.1069 \[cond-mat.str-el\]](#).
- [4] H. H. Zhao, Z. Y. Xie, Q. N. Chen, Z. C. Wei, J. W. Cai, and T. Xiang, “Renormalization of tensor-network states,” *Phys. Rev. B* **81** no. 17, (2010) 174411, [arXiv:1002.1405 \[cond-mat.str-el\]](#).
- [5] Z. Y. Xie, J. Chen, M. P. Qin, J. W. Zhu, L. P. Yang, and T. Xiang, “Coarse-graining renormalization by higher-order singular value decomposition,” *Phys. Rev. B* **86** no. 4, (2012) 045139, [arXiv:1201.1144 \[cond-mat.stat-mech\]](#).
- [6] G. Evenbly and G. Vidal, “Tensor Network Renormalization,” *Phys. Rev. Lett.* **115** no. 18, (2015) 180405, [arXiv:1412.0732 \[cond-mat.str-el\]](#).
- [7] S. Yang, Z.-C. Gu, and X.-G. Wen, “Loop Optimization for Tensor Network Renormalization,” *Phys. Rev. Lett.* **118** no. 11, (2017) , [arXiv:1512.04938 \[cond-mat.str-el\]](#).
- [8] M. Bal, M. Mariën, J. Haegeman, and F. Verstraete, “Renormalization group flows of Hamiltonians using tensor networks,” *Phys. Rev. Lett.* **118** (2017) 250602, [arXiv:1703.00365 \[cond-mat.stat-mech\]](#).

- [9] G. Evenbly, “Implicitly disentangled renormalization,” [arXiv:1707.05770 \[quant-ph\]](#).
- [10] M. Hauru, C. Delcamp, and S. Mizera, “Renormalization of tensor networks using graph independent local truncations,” *Phys. Rev. B* **97** no. 4, (2018) 045111, [arXiv:1709.07460 \[cond-mat.str-el\]](#).
- [11] T. Yamashita and T. Sakurai, “A parallel computing method for the higher order tensor renormalization group,” *Computer Physics Communications* **278** (2022) 108423, [arXiv:2110.03607 \[hep-lat\]](#).
- [12] X. Lyu and N. Kawashima, “Essential difference between 2D and 3D from the perspective of real-space renormalization group,” [arXiv:2311.05891 \[cond-mat.stat-mech\]](#).
- [13] T. Kennedy and S. Rychkov, “Tensor RG Approach to High-Temperature Fixed Point,” *J. Statist. Phys.* **187** no. 3, (2022) 33, [arXiv:2107.11464 \[math-ph\]](#).
- [14] T. Kennedy and S. Rychkov, “Tensor Renormalization Group at Low Temperatures: Discontinuity Fixed Point,” *Annales Henri Poincaré* **25** no. 1, (2024) 773–841, [arXiv:2210.06669 \[math-ph\]](#).
- [15] N. Ebel, “3D Tensor Renormalisation Group at High Temperatures,” *Annales Henri Poincaré* (July, 2024), [arXiv:2401.04229 \[cond-mat.stat-mech\]](#).
- [16] G. Evenbly and G. Vidal, “Local Scale Transformations on the Lattice with Tensor Network Renormalization,” *Phys.Rev.Lett.* **116** no. 4, (2016) 040401, [arXiv:1510.00689 \[cond-mat.str-el\]](#).
- [17] K. Wilson and J. B. Kogut, “The Renormalization group and the epsilon expansion,” *Phys.Rept.* **12** (1974) 75–200.
- [18] F. Wegner, “The Critical State, General Aspects,” in *Phase Transitions and Critical Phenomena, Vol.6*, C. Domb and M. Green, eds., pp. 8–126. Academic Press, 1976.
- [19] X. Lyu, R. G. Xu, and N. Kawashima, “Scaling dimensions from linearized tensor renormalization group transformations,” *Phys. Rev. Res.* **3** no. 2, (2021) 023048, [arXiv:2102.08136 \[cond-mat.stat-mech\]](#).
- [20] W. Guo and T.-C. Wei, “Tensor network methods for extracting conformal field theory data from fixed-point tensors and defect coarse graining,” *Phys. Rev. E* **109** (2024) 034111, [arXiv:2305.09899 \[cond-mat.stat-mech\]](#).
- [21] N. Ebel, T. Kennedy, and S. Rychkov, “Transfer Matrix and Lattice Dilatation Operator for High-Quality Fixed Points in Tensor Network Renormalization Group,” [arXiv:2409.13012 \[cond-mat.stat-mech\]](#).
- [22] G. Evenbly, “Algorithms for tensor network renormalization,” [arXiv:1509.07484 \[cond-mat.str-el\]](#).
- [23] M. Levin, “Real space renormalization group and the emergence of topological order,” talk at the workshop ‘Topological Quantum Computing’, Institute for Pure and Applied Mathematics, UCLA, February 26-March 2, 2007.
- [24] A. Ueda and M. Yamazaki, “Fixed-point tensor is a four-point function,” [arXiv:2307.02523 \[hep-th\]](#).
- [25] A. Ueda, “Renormalization group flow and fixed-point in tensor network representations,” [arXiv:2401.18068 \[cond-mat.stat-mech\]](#). PhD thesis (Univ. of Tokyo).

- [26] G. Cheng, L. Chen, Z.-C. Gu, and L.-Y. Hung, “Exact fixed-point tensor network construction for rational conformal field theory,” [arXiv:2311.18005 \[cond-mat.str-el\]](#).
- [27] N. Ebel, T. Kennedy, and S. Rychkov, “Renormalization Group with Tensor Networks: Exact Fixed Points, Hilbert-Schmidt Condition, and Necessity of Disentangling,”. to appear.
- [28] P. Di Francesco, P. Mathieu, and D. Senechal, *Conformal field theory*. Springer, 1997.
- [29] M. Hauru, G. Evenbly, W. W. Ho, D. Gaiotto, and G. Vidal, “Topological conformal defects with tensor networks,” *Phys. Rev. B* **94** no. 11, (2016) 115125, [arXiv:1512.03846 \[cond-mat.str-el\]](#).
- [30] G. Evenbly, “Example codes: TNR.” <https://www.tensors.net/tnr>. Accessed: 2024-03-23.
- [31] [https://github.com/ebelnikola/GILT\\_TNR\\_R](https://github.com/ebelnikola/GILT_TNR_R).
- [32] “Gilt-TNR.” <https://github.com/Gilt-TNR/Gilt-TNR>.
- [33] K. Homma, T. Okubo, and N. Kawashima, “Nuclear norm regularized loop optimization for tensor network,” [arXiv:2306.17479 \[cond-mat.stat-mech\]](#).
- [34] “Julia.” <https://julialang.org/>.
- [35] J. Bezanson, A. Edelman, S. Karpinski, and V. B. Shah, “Julia: A fresh approach to numerical computing,” *SIAM Review* **59** no. 1, (2017) 65–98.
- [36] J. Haegeman, “Krylovkit,” 2024. <https://github.com/Jutho/KrylovKit.jl>.
- [37] A. Acuaviva, V. Makam, H. Nieuwboer, D. Pérez-García, F. Sittner, M. Walter, and F. Witteveen, “The minimal canonical form of a tensor network,” in *2023 IEEE 64th Annual Symposium on Foundations of Computer Science (FOCS)*, pp. 328–362. 2023. [arXiv:2209.14358 \[quant-ph\]](#).
- [38] G. Evenbly, “TensorTrace.” <https://www.tensortrace.com/>. Accessed: 2024-07-17.
- [39] Wikipedia, “Automatic differentiation,” [https://en.wikipedia.org/wiki/Automatic\\_differentiation](https://en.wikipedia.org/wiki/Automatic_differentiation).
- [40] <https://github.com/brucelyu/tensorRGflow/tree/main>.
- [41] C. Fieker, W. Hart, T. Hofmann, and F. Johansson, “Nemo/Hecke: Computer Algebra and Number Theory Packages for the Julia Programming Language,” in *Proceedings of the 2017 ACM on International Symposium on Symbolic and Algebraic Computation, ISSAC ’17*, pp. 157–164. ACM, New York, NY, USA, 2017.
- [42] “AbstractAlgebra.jl.” <https://github.com/Nemocas/AbstractAlgebra.jl>.
- [43] W. H. Press, S. A. Teukolsky, W. T. Vetterling, and B. P. Flannery, *Numerical Recipes 3rd Edition: The Art of Scientific Computing*. Cambridge University Press, 2007.